Versatile Reactivity of Mn-II Complexes in Reactions with N-Donor Heterocycles: Metamorphosis of Labile Homometallic Pivalates vs. Assembling of Endurable Heterometallic Acetates

Ruslan A. Polunin, Igor S. Evstifeev, Olivier Cador, Stéphane Golhen, Konstantin S. Gavrilenko, Anton S. Lytvynenko, Nikolay N. Efimov, Vadim V. Minin, Artem S. Bogomyakov, Lahcène Ouahab, et al.

molecules

MDPI

Article

Versatile Reactivity of Mn^{II} Complexes in Reactions with N-Donor Heterocycles: Metamorphosis of Labile Homometallic Pivalates vs. Assembling of Endurable Heterometallic Acetates

Ruslan A. Polunin [1,†], Igor S. Evstifeev [2], Olivier Cador [3,*], Stéphane Golhen [3], Konstantin S. Gavrilenko [4,5], Anton S. Lytvynenko [1], Nikolay N. Efimov [2], Vadim V. Minin [2], Artem S. Bogomyakov [6], Lahcène Ouahab [3], Sergey V. Kolotilov [1,*], Mikhail A. Kiskin [2,*] and Igor L. Eremenko [2]

1 L. V. Pisarzhevskii Institute of Physical Chemistry of the National Academy of Sciences of Ukraine, Prospekt Nauki 31, 03028 Kiev, Ukraine; anton.s.lytvynenko@gmail.com
2 N. S. Kurnakov Institute of General and Inorganic Chemistry, Russian Academy of Sciences, Leninsky Prosp. 31, 119991 Moscow, GSP-1, Russia; i.evstifeev@gmail.com (I.S.E.); nnefimov@yandex.ru (N.N.E.); minin@igic.ras.ru (V.V.M.); ilerem@igic.ras.ru (I.L.E.)
3 University of Rennes, CNRS, Institut des Sciences Chimiques de Rennes (ISCR)–UMR 6226, F-35000 Rennes, France; stephane.golhen@univ-rennes1.fr (S.G.); lahcene.ouahab@univ-rennes1.fr (L.O.)
4 Research-And-Education ChemBioCenter, National Taras Shevchenko University of Kyiv, Chervonotkatska str., 61, 03022 Kiev, Ukraine; kgavrio@gmail.com
5 Enamine Ltd. 78 Chervonotkatska str., 02660 Kiev, Ukraine
6 International Tomography Center, Siberia Branch of Russian Academy of Science, Institutskaya str. 3a, 630090 Novosibirsk, Russia; bus@tomo.nsc.ru
* Correspondence: olivier.cador@univ-rennes1.fr (O.C.); s.v.kolotilov@gmail.com (S.V.K.); mkiskin@igic.ras.ru (M.A.K.)
† Deceased.

Abstract: Reaction of 2,2′-bipyridine (2,2′-bipy) or 1,10-phenantroline (phen) with $[Mn(Piv)_2(EtOH)]_n$ led to the formation of binuclear complexes $[Mn_2(Piv)_4L_2]$ (L = 2,2′-bipy (**1**), phen (**2**); Piv^- is the anion of pivalic acid). Oxidation of **1** or **2** by air oxygen resulted in the formation of tetranuclear $Mn^{II/III}$ complexes $[Mn_4O_2(Piv)_6L_2]$ (L = 2,2′-bipy (**3**), phen (**4**)). The hexanuclear complex $[Mn_6(OH)_2(Piv)_{10}(pym)_4]$ (**5**) was formed in the reaction of $[Mn(Piv)_2(EtOH)]_n$ with pyrimidine (pym), while oxidation of **5** produced the coordination polymer $[Mn_6O_2(Piv)_{10}(pym)_2]_n$ (**6**). Use of pyrazine (pz) instead of pyrimidine led to the 2D-coordination polymer $[Mn_4(OH)(Piv)_7(\mu_2\text{-}pz)_2]_n$ (**7**). Interaction of $[Mn(Piv)_2(EtOH)]_n$ with $FeCl_3$ resulted in the formation of the hexanuclear complex $[Mn^{II}_4Fe^{III}_2O_2(Piv)_{10}(MeCN)_2(HPiv)_2]$ (**8**). The reactions of $[MnFe_2O(OAc)_6(H_2O)_3]$ with 4,4′-bipyridine (4,4′-bipy) or *trans*-1,2-(4-pyridyl)ethylene (bpe) led to the formation of 1D-polymers $[MnFe_2O(OAc)_6L_2]_n \cdot 2n$DMF, where L = 4,4′-bipy (**9**·2DMF), bpe (**10**·2DMF) and $[MnFe_2O(OAc)_6(bpe)(DMF)]_n \cdot 3.5n$DMF (**11**·3.5DMF). All complexes were characterized by single-crystal X-ray diffraction. Desolvation of **11**·3.5DMF led to a collapse of the porous crystal lattice that was confirmed by PXRD and N_2 sorption measurements, while alcohol adsorption led to porous structure restoration. Weak antiferromagnetic exchange was found in the case of binuclear Mn^{II} complexes ($J_{Mn\text{-}Mn} = -1.03$ cm^{-1} for **1** and **2**). According to magnetic data analysis ($J_{Mn\text{-}Mn} = -(2.69 \div 0.42)$ cm^{-1}) and DFT calculations ($J_{Mn\text{-}Mn} = -(6.9 \div 0.9)$ cm^{-1}) weak antiferromagnetic coupling between Mn^{II} ions also occurred in the tetranuclear $\{Mn_4(OH)(Piv)_7\}$ unit of the 2D polymer **7**. In contrast, strong antiferromagnetic coupling was found in oxo-bridged trinuclear fragment $\{MnFe_2O(OAc)_6\}$ in **11**·3.5DMF ($J_{Fe\text{-}Fe} = -57.8$ cm^{-1}, $J_{Fe\text{-}Mn} = -20.12$ cm^{-1}).

Keywords: polynuclear complexes; manganese; pyridines; coordination polymers; porous materials; magnetic properties

Citation: Polunin, R.A.; Evstifeev, I.S.; Cador, O.; Golhen, S.; Gavrilenko, K.S.; Lytvynenko, A.S.; Efimov, N.N.; Minin, V.V.; Bogomyakov, A.S.; Ouahab, L.; et al. Versatile Reactivity of Mn^{II} Complexes in Reactions with N-Donor Heterocycles: Metamorphosis of Labile Homometallic Pivalates vs. Assembling of Endurable Heterometallic Acetates. *Molecules* **2021**, *26*, 1021. https://doi.org/10.3390/molecules26041021

Academic Editor: Nikolay Gerasimchuk
Received: 16 January 2021
Accepted: 11 February 2021
Published: 15 February 2021

1. Introduction

Polynuclear coordination compounds of transition metals are widely used as catalysts in various reactions [1–5], as starting materials for the preparation of nanosized oxides

or metals [6–8], as well as the basis for the creation of new magnetic materials [9–13] and coordination polymers with remarkable properties [14–20]. In the majority of these applications the stability or reactivity of the polynuclear core play an important role. In many cases polynuclear complexes undergo rearrangement or dissociation in solution because of instability in solvent or upon interaction with the "additional" ligands [21–27], and the resulting compounds may contain a metal core different from the one existing in the starting complex. Such rearrangement reactions lead to the formation of certain polynuclear cores, which are most stable under the reaction conditions. For example, binuclear cores $M_2(O_2CR)_4$ (M^{II} = Cu, Zn, Co, Ni) [28], trinuclear cores Fe^{III}_3 or $Fe^{III}_2M^{II}$ (M = Ni, Co, Mn) [29–32], $M^{II}_2Ln^{III}$ (M^{II} = Zn, Co, Ni; Ln is lanthanide) [33–35] often form due to their exceptional stability in various media. However, the result of such rearrangements is not always predictable, since many factors may influence the reaction pathway.

In this work manganese complexes were chosen as the objects of research due to some specific features of this ion, which are manifested in the reactivity of its polynuclear complexes [25,26]. The reasons for such differences include the wide range of stable oxidation states of manganese with low energy barriers for redox-transformations [36,37], as well as, in the case of Mn^{II}, the relatively high kinetic lability of this ion [36]. The additional reasons for interest to homo- and heterometallic manganese complexes is that such species have found applications as building blocks for the synthesis of single-molecule magnets [9,15,38] or various coordination polymers capable of absorbing guest molecules [39,40]. It is also known that molecular manganese compounds can oligomerize upon crystallization during solvent changes, giving rise to complexes with higher nuclearity [9,26,26].

The aim of this study was to reveal the stability limits of Mn^{II} homometallic (pivalate) or heterometallic (Fe_2Mn acetate) complexes in reactions with N-donor ligands (Scheme 1) and to compare the reactivity of Mn^{II} species with the reactivity of Ni^{II} and Co^{II} analogues. An additional aim of the study was to see the influence of the structure of new compounds on their ability to uptake guest molecules or on the magnetic exchange interactions in the polymetallic cores.

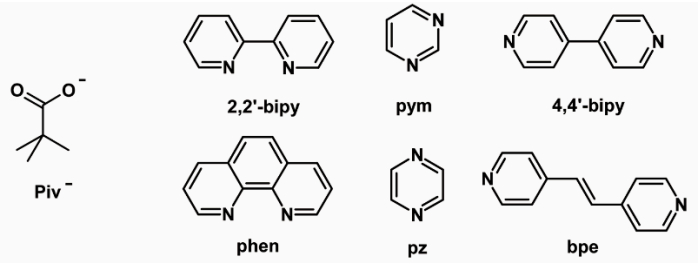

Scheme 1. Formulae of pivatale (Piv^-) and N-donor ligands used in the study.

In this study we used pivalate manganese(II) polymer $[Mn(Piv)_2(EtOH)]_n$ and trinuclear manganese(II)-iron(III) oxoacetate $[MnFe_2O(OAc)_6(H_2O)_3]_n$ (Piv^- is the anion of pivalic acid) as starting compounds. Reactions of $[Mn(Piv)_2(EtOH)]_n$ with both chelating (2,2′-bipyridine (2,2′-bipy) and 1,10-phenantroline (phen)) and non-chelating bridging (pyrimidine (pym), pyrazine (pz)) N-donor ligands in the absence/presence of oxygen as oxidant were investigated. In contrast to Ni^{II} and Co^{II}, the reaction of Mn^{II} pivalate with $FeCl_3$ led to formation of a compound with a $Mn_4Fe_2O_2(Piv)_{10}$ core. Reaction of the same Mn^{II} pivalate with a N-donor ligand led to the assembly of various polynuclear cores, while reaction of $Fe^{III}_2Mn^{II}$ acetate with N-donors of the pyridine type led to the formation of new complexes where the trinuclear $Fe^{III}_2Mn^{II}$ core was preserved. The crystal and molecular structures of eleven new compounds were determined—$[Mn_2(Piv)_4L_2]$ (L = 2,2′-bipy (**1**), phen (**2**)), $[Mn_4O_2(Piv)_6L_2]\cdot MeCN$ (L = 2,2′-bipy (**3**·MeCN), phen (**4**·0.5MeCN)), $[Mn_6(OH)_2(Piv)_{10}(pym)_4]$ (**5**), $[Mn_6O_2(Piv)_{10}(pym)_2]_n$ (**6**), $[Mn_4(OH)(Piv)_7(pz)_2]_n\cdot 2n$MeCN (**7**·2MeCN), $[Mn_4Fe_2O_2(Piv)_{10}(MeCN)_2(HPiv)_2]\cdot 2MeCN$ (**8**·2MeCN), $[MnFe_2O(OAc)_6L_2]_n\cdot 2n$DMF (L = 4,4′-bipy (**9**·2DMF), bpe (**10**·2DMF), $[MnFe_2O(OAc)_6(bpe)(DMF)]_n\cdot 4n$DMF (**11**·3.5DMF). Sorption of alcohols by porous coordination poly-

mers, as well as the magnetic properties of several polynuclear Mn-containing complexes were studied.

2. Results and Discussion

2.1. Synthesis

The reaction of $[Mn(Piv)_2(EtOH)]_n$ and 2,2′-bipyridine (2,2′-bipy) or 1,10-phenantroline (phen) in MeCN under an argon atmosphere led to formation of molecular complexes $[Mn_2^{II}(Piv)_4L_2]$ (L = 2,2′-bipy (**1**), phen (**2**), Figure 1). Oxidation of these complexes or the initial reaction system resulted in rearrangement of the dinuclear molecules to tetranuclear complexes $[Mn_2^{II}Mn_2^{III}O_2(Piv)_6L_2]$ (L = 2,2′-bipy (**3**), phen (**4**)).

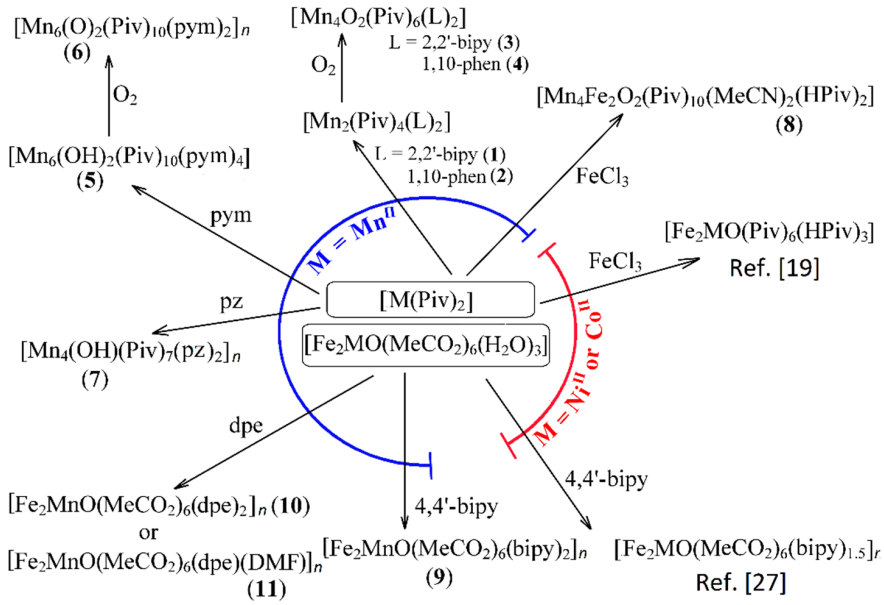

Figure 1. Scheme illustrating the formation of complexes **1**–**11**. 2,2′-bipy is 2,2′-bipyridine, 4,4′-bipy is 4,4′-bipyridine, bpe is 1,2-bis-*trans*-(4-pyridyl)ethylene, pym = pyrimidine, pz = pyrazine. $M(Piv)_2$ in the center of the scheme means $[Mn(Piv)_2(EtOH)]_n$ or $Ni(Piv)_2(H_2O)_2$ or $[Co(Piv)_2]_n$.

Binuclear complexes **1** and **2** are similar to reported binuclear complexes of other *d*-metals with +2 charge [41–48]. The complex **3** is known and was obtained earlier by reaction of $[Mn(Piv)_2(EtOH)]_n$ and 2,2′-bipy in THF in air [49].

Reaction of $[Mn(Piv)_2(EtOH)]_n$ and pyrimidine (pym) in MeCN under an argon atmosphere led to the molecular hexanuclear complex $[Mn_6(OH)_2(Piv)_{10}(pym)_4]$ (**5**). On exposure to air in MeCN compound **5** was oxidized to give the 1D polymer $[Mn^{II}_4Mn^{III}_2(\mu_4\text{-}O)_2(Piv)_{10}(\mu_2\text{-}pym)(pym)]_n$ (**6**).

Previously reported carboxylate complexes of transition metals ions formed polymeric compounds with pyrimidine [50], so the formation of the molecular complex **5** is uncommon. At the same time, the formation of the mixed valence hexanuclear fragment $\{Mn^{II}_4Mn^{III}_2(\mu_4\text{-}O)_2(Piv)_{10}\}$ is similar to that in **5** and quite typical, for example, oxidation of $[Mn(Piv)_2(EtOH)]_n$ (the same starting compound as in formation of **5**) by air led to $[Mn^{II}_4Mn^{III}_2(\mu_4\text{-}O)_2(Piv)_{10}(HPiv)(EtOH)_3]$ [51]; a similar hexanuclear Mn_6 core was found in polymeric compounds [40,52]. Introduction of pyrimidine ligands resulted in formation of new coordination polymers.

The use of pyrazine (pz) instead of pyrimidine in the reaction with $[Mn(Piv)_2(EtOH)]_n$ in MeCN under an argon atmosphere led to the formation of the 2D-coordination polymer $[Mn_4(OH)(Piv)_7(\mu_2\text{-}pz)_2]_n$ (**7**). This complex was stable in air and was not soluble in MeCN, and this reason probable precluding oxidation of Mn^{II}. Pyrazine is a quite typical bridging ligand in the chemistry of manganese, forming polymers with Mn^{II} carboxylates [53,54], as well as with the mixed-valence hexanuclear fragment $\{Mn^{II}_4Mn^{III}_2(\mu_4\text{-}$

$O)_2(O_2CR)_{10}\}$ [54–56]. From an analysis of literature, as well as from the results of this study it can be noted that the tetranuclear unit $\{Mn^{II}_2Mn^{III}_2O_2(O_2CR)_6\}$ usually forms in the presence of chelating ligands, such as 2,2′-bipy and phen, while the hexanuclear unit $\{Mn^{II}_4Mn^{III}_2O_2(O_2CR)_{10}\}$ is produced in reactions with monodentate N-donor ligands or in the absence of such ligands.

It is known that the M^{II} ions (such as Mn^{II}, Co^{II} or Ni^{II}) and Fe^{III} ions quite typically form trinuclear acetates $[Fe_2MO(OAc)_6(H_2O)_3]$ [30]. Earlier we reported that Co^{II} and Ni^{II} pivalates with $FeCl_3{\cdot}6H_2O$ in acetonitrile gave similar trinuclear complexes $[Fe_2MO(Piv)_6(HPiv)_3]$ (M = Co, Ni) [19]. Unexpectedly, $[Mn(Piv)_2(EtOH)]_n$ reacted with $FeCl_3{\cdot}6H_2O$ in MeCN under an argon atmosphere with formation of the hexanuclear complex $[Mn^{II}_4Fe^{III}_2O_2(Piv)_{10}(MeCN)_3]$ (**8**). On the other hand, with an excess of pivalic acid in the reaction of $FeCl_3{\cdot}6H_2O$, $Mn(NO_3)_2{\cdot}6H_2O$ and KOH $[Mn^{II}Fe^{III}_2O(Piv)_6(HPiv)_3]$ is formed [57]. The trinuclear fragments $\{Fe_2MnO(Piv)_6\}$ were also generated in situ in the synthesis of coordination polymers [58].

The synthesis of compounds **9**–**11** was based on substitution of coordinated water molecules in $[Fe_2MnO(OAc)_6(H_2O)_3]$ by 4,4′-bipyridine (4,4′-bipy) or 1,2-*trans*-(4-pyridyl)ethene (bpe). In compounds **9** and **10** all vacancies in the coordination spheres of the metal ions are filled by the nitrogen atoms of 4,4′-bipy or bpe ligands, while 4,4′-bipy or bpe molecules act both as bridging and non-bridging (capping) ligands, as will be described in details in the X-ray structures description (vide infra). In compound **11** all bpe molecules link trinuclear blocks but only two of three possible "vacant" positions in the coordination spheres of metal ions are occupied by a pyridine group of bpe; the third position is filled by DMF.

Formation of coordination polymers **9**–**11** can be formally described as the generation of a 1D-chain of $[MnFe_2O(OAc)_6(L)]_n$ (L = 4,4′-bipy or bpe) and filling of the third positions by terminal 4,4′-bipy and $[MnFe_2O(OAc)_6(4,4'\text{-bipy})_3]_n$ (for **9**), by bpe or DMF (for **10** and **11**, respectively). Synthesis of compounds $[M_3O(RCO_2)_6(4,4'\text{-bipy})_3]^{0/+}$ which can potentially bind metal ions was reported earlier [59]. In contrast to the reaction of $[Fe_2MO(OAc)_6(H_2O)_3]$ (M = Co, Ni) with 4,4′-bipy which led to destruction of the trinuclear blocks or to the formation of porous $[MFe_2O(OAc)_6(4,4'\text{-bipy})_{1.5}]_n$ coordination polymers [27], compound $[Fe_2MO(OAc)_6(H_2O)_3]$ was stable under the same conditions and formed coordination polymers with a ratio of trinuclear block to bridging ligand equal to 1:1 or 1:2.

2.2. Crystal and Molecular Structures

The crystal structures of molecular complexes **1**–**5**, **8** and coordination polymers **6**, **7**, **9**–**11** were determined by single crystal X-ray analysis.

2.2.1. Compounds **1** and **2**

Complexes **1** and **2** have dinuclear cores (Mn . . . Mn 4.448(2) and 4.015(3) Å, respectively) with a common metal-carboxylate fragment $\{Mn_2(\mu\text{-Piv})_2(\eta\text{-Piv})_2\}$. Despite their similar composition, the structures of these fragments are different (Figure 2a,b). The binuclear complex in **1** is centrosymmetric (the inversion center lies between the metal atoms), while compound **2** possesses axial symmetry (a 2_1 axis passes between the metal atoms). In both **1** and **2** oxygen donors occupy four positions in the coordination sphere of each of Mn^{II} ion, and two N atoms from 2,2′-bipy or phen complete the coordination spheres of these ions to form distorted octahedra (Figure 2a,b). The Mn–O and Mn–N bond lengths in **1** and **2** fall in range 2.039(4)–2.607(6) Å and 2.263(4)–2.342(4) Å respectively, which is typical for complexes of Mn^{II} with carboxylates and 2,2′-bipy or phen [44,45,60–62].

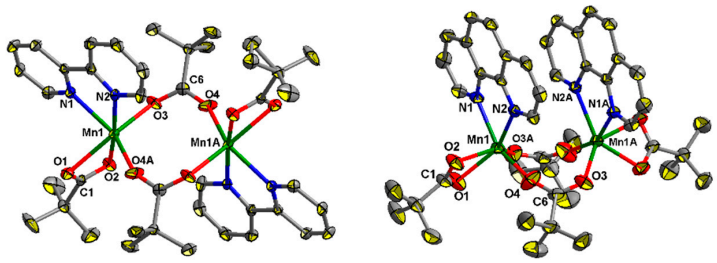

(**a**) (**b**)

Figure 2. The molecular structures of **1** ((**a**), atoms with an additional character in the atom labels are at $(1 - x, 1 - y, 2 - z)$) and **2** ((**b**), atoms with an additional character in the atom labels are at $(1 - x, y, 1/2 - z)$)H atoms at carbon atoms are omitted for clarity, the displacement ellipsoids are drawn at the 30% probability level.

To the best of our knowledge, the dinuclear core in **1** is the first example of a Mn_2 structural unit block possessing a *syn*,*syn*-binding μ-COO-group and chelating 2,2′-bipy ligands. A compound of similar composition, $Mn_2(ad(O_2C)_2)_2(2,2'\text{-bipy})_2 \cdot 0.5H_2O$ (where $ad(O_2C)_2^{2-}$ is 1,3-adamantanedicarboxylate) [60] contained a dinuclear $Mn_2(\mu_2\text{-}O_2C)_2(\eta\text{-}O_2C)_2$ unit with *syn*,*anti*-coordination mode of the μ-O_2C-groups.

The aromatic rings of 2,2′-bipy ligands of the neighboring molecules in **1** are not parallel, and the angle between the mean planes of these molecules is 7.6(3)°. The closest distance between centroids of pairs rings of different 2,2′-bipy ligands is 3.591(4) Å (the slippage is 0.707 Å). This leads to the formation of a supramolecular chain along the *c* axis (Figure 3b), probably due to π-stacking interactions.

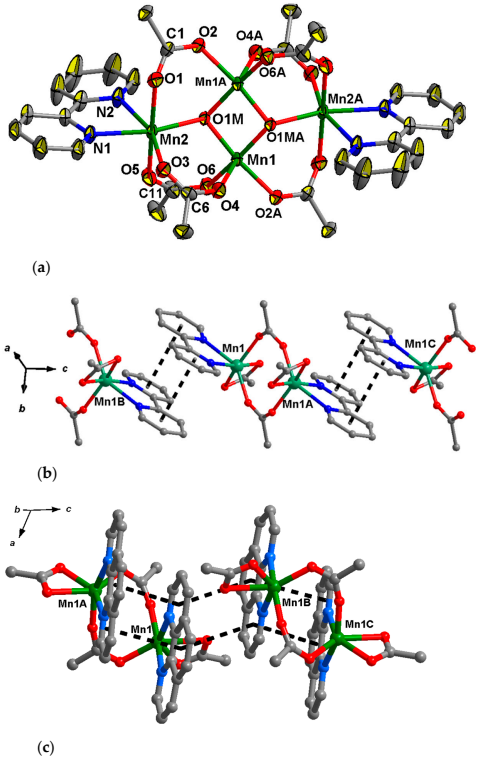

Figure 3. , The molecular structure of **3** ((**a**), atoms with an additional character in the atom labels are at $(-x, 1 - y, 1 - z)$), intra- (only for **2**) and intermolecular (for **1** and **2**) π-stacking interaction and formation of supramolecular chain structure in crystal lattices of **1** (**a**) and **2** (**b**) (H atoms at carbon atoms and methyl groups of pivalate ions are omitted for clarity, (**c**) the displacement ellipsoids are drawn at the 30% probability level).

The aromatic rings of two phen ligands in one molecule of **2** are not parallel, and the angle between the mean planes of these molecules is 9.8(2)°. The closest distance between centroids of pairs rings (N2C18-C22, C14-C19), belonging to these different phen ligands, is 3.695(4) Å (the slippage is 1.055 Å). The mean planes of phen ligands from the neighboring different molecules of **2** are parallel and the centroids of these pairs of phen rings are located in 3.730(4) Å (the slippage is 1.561 Å). Such an arrangement of aromatic phen molecules can allow for π-stacking interactions between them and as a result formation of a supramolecular pile structure along the *c* axis (Figure 3c). However, it cannot be excluded that intramolecular π-stacking between phen molecules in **2** may be the reason for the difference between structures of this compound and **1**: the 2,2′-bipy molecules in **1** are located on different sides in respect to the inversion center, located between the Mn^{II} ions.

2.2.2. Compounds **3** and **4**

The molecules of compounds **3** and **4** are centrosymmetric (an inversion center lies between the central metal ions) and possess a similar tetranuclear $Mn_4O_2(Piv)_6$ core (Figure 3a) of a "butterfly" type, which is quite typical for Mn carboxylates [63–66]. Each Mn^{III} ion in the center of the butterfly is located in a square pyramidal coordination polyhedron (MnO_5 chromofore, τ = 0.15 [63–66]), while Mn^{II} ions on the wings of the butterfly are hexacoordinate and donor atoms in their coordination environment form highly distorted octahedra (MnO_4N_2 chromophores, where N atoms belong to 2,2′-bipy or phen in **3** and **4**, respectively). Mn^{III}–(μ$_3$–O) and Mn^{II}–(μ$_3$–O) bond lengths in **3** and **4** fall in range 1.843(2)–1.851(2) Å and 2.073(3)–2.099(2) Å, respectively, which is typical for Mn-O distances within trinuclear units $Mn^{II}_2Mn^{III}_2O_2$ [63–66]. Mn^{III}–O and Mn^{II}–O (O atoms from pivalate) bond lengths fall in range 1.957(2)–2.097(2) and 2.116(2)–2.213(3) respectively for **3**, and 1.955(3)–2.105(3) Å and 2.105(3)–2.196(3) Å respectively for **4**, making these bonds longer than the corresponding bonds of Mn ions with μ$_3$-O atoms. Terminal Mn^{II} atoms fill up their coordination sphere by coordination of 2,2′–bipy or phen with Mn–N bond lengths 2.271(3), 2.284(3) Å for **3**, and 2.256(4), 2.284(4) Å for **4**.

2.2.3. Compound **5**

Compound **5** crystallizes in the monoclinic space group $P2_1/n$ as a discrete centrosymmetric hexanuclear complex (the inversion center lies between the central metal ions Mn2, Mn3, Mn2A and Mn3A). The hexanuclear core of **5** can be considered as two identical triangular fragments {Mn_3(OH)(Piv)$_3$(pym)$_2$} linked by four carboxylic acid groups (two μ$_2$-Piv and two μ$_3$-Piv) (Figure 4a). In each trinuclear fragment Mn^{II} ions are linked by μ$_3$-OH (bond lengths Mn–O are equal to 2.049(2)–2.184(2) Å), and the O atom is located on 0.66(2) Å above the Mn1Mn2Mn3 plane, which can be an additional proof that the central oxygen atom belongs to a μ$_3$-hydroxo group rather than a μ$_3$-oxo (Mn_3(μ$_3$-O) unit that is expected to be planar [67–70]). One μ-O_2C bridging group links Mn1 and Mn2, and two μ$_2$-O_2C groups link Mn1 with Mn3 (bond lengths Mn–O(Piv) and lie in the 2.095(3)–2.142(3) Å) range. In addition to the oxygen atoms of carboxylate groups, the nitrogen atoms of two pyrimidine molecules are coordinated to Mn1, completing its coordination polyhedron to form a distorted octahedron (Mn1–N bond lengths are 2.293(3) and 2.322(3) Å). Mn2 is located in the distorted tetrahedral donor set O_4 (Mn2–O(Piv) bond lengths are in range 2.067(3)–2.097(3) Å)), and Mn3 is in a distorted octahedral donor set O_6 (Mn3–O(Piv) bond lengths are in range 2.094(3)–2.262(2) Å)).

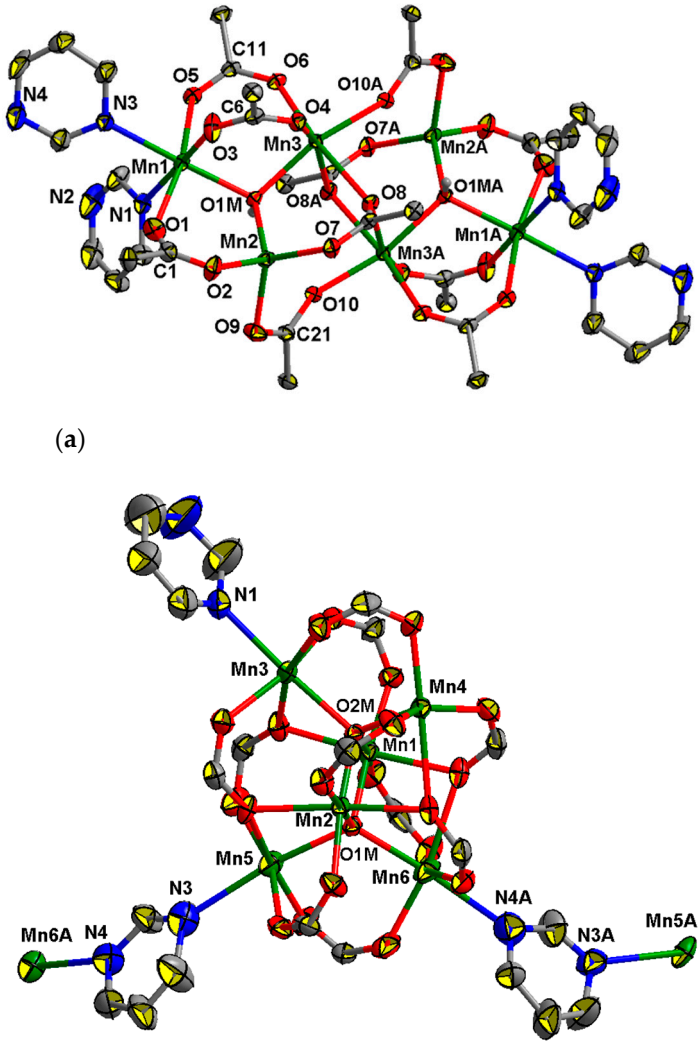

Figure 4. Structures of polynuclear units in **5** (**a**) and **6** (**b**) respectively. H atoms at carbon atoms, and methyl (in **5**) and *tert*-butyl (in **6**) groups of pivalate ions are omitted for clarity, the displacement ellipsoids are drawn at the 30% probability level).

2.2.4. Compound **6**

This compound crystallizes as a 1D polymer in the space group *Pn*, in which hexanuclear units $\{Mn^{II}_4Mn^{III}_2O_2(Piv)_{10}\}$ are linked by pyrimidine bridges (Figure 4b). Generally, the structure of the Mn_6 core in **6** is similar to that of the hexanuclear units observed in $[M^{II}_4M^{III}_2(O)_2(O_2CR)_{10}(L)_4]$ complexes, where L is a neutral N- or O-donor ligands [71–74] with the difference that one Mn4 atom in **6** possesses coordination number four and is located in a coordination polyhedron, close to a distorted square-pyramid ($\tau = 0.12$) [75]. Central Mn^{III} ions (Mn1 … Mn2 2.835(3) Å) possess O_6 donor sets (Mn–O(μ_4–O) 1.878(7)–1.914(8) Å, Mn–O 1.933(9)–2.267(9) Å), three of four terminal Mn^{II} ions are located in O_5N donor sets (Mn–O(μ_4–O) 2.019(8)–2.200(8) Å, Mn–O 1.970(10)–2.457(10) Å, Mn3–N1 2.255(12), Mn5–N3 2.511(16), Mn6–N4 2.471(18) Å), where N is an atom of a bridging (N3 and N4) or non-bridging (N1) pyrimidine molecule. In the crystal lattice 1D chains of **6** are arranged parallel to the *a* axis. The crystal lattice of **6** is retained upon sample storage in air, as confirmed by powder XRD (Figure S1, Supporting information).

2.2.5. Compound **7**

This complex crystallizes in the triclinic space group *P*-1 as a solvate with two molecules of MeCN. The tetranuclear core $\{Mn^{II}_4(OH)(Piv)_7\}$ (Figure 5a) in **7** can be described as a trinuclear μ_3-hydroxo-centered unit $Mn_3(OH)(Piv)_4$ (Mn … Mn 3.371(2)–3.735(2) Å), linked with the fourth Mn4 ion (Mn4 … Mn 3.451(2), 4.157(2) Å) by four pivalate anions. Such a Mn_4 unit is not symmetric. The $Mn_3(OH)(Piv)_4$ bond lengths of Mn–O1M fall in the 2.131(2)–2.134(2) Å range, with atom O1M located above Mn1Mn2Mn3 plane at 0.64(3) Å, *d*(Mn–O(Piv) = 2.111(3)–2.238(3) Å. The Mn1 ion is bound to two pyrazine ligands (Mn1–N = 2.346(4), 2.389(4) Å), while the Mn3 and Mn4 ions are bound to one molecule of pyrazine (Mn3–N 2.277(4) Å, Mn4–N 2.315(4) Å). Thus, the Mn1, Mn2 and Mn3 ions possess distorted octahedral donor sets O_4N_2, O_6 and O_5N, respectively, and the Mn4 ion is located in a distorted square-pyramidal coordination environment (O_4N donor set; τ = 0.08) [75]. All pyrazine molecules in **7** are bridging. Local symmetry centers of the unit cell are located in the centers of the pyrazine rings which link Mn1-Mn1′ and Mn3-Mn3′ ions.

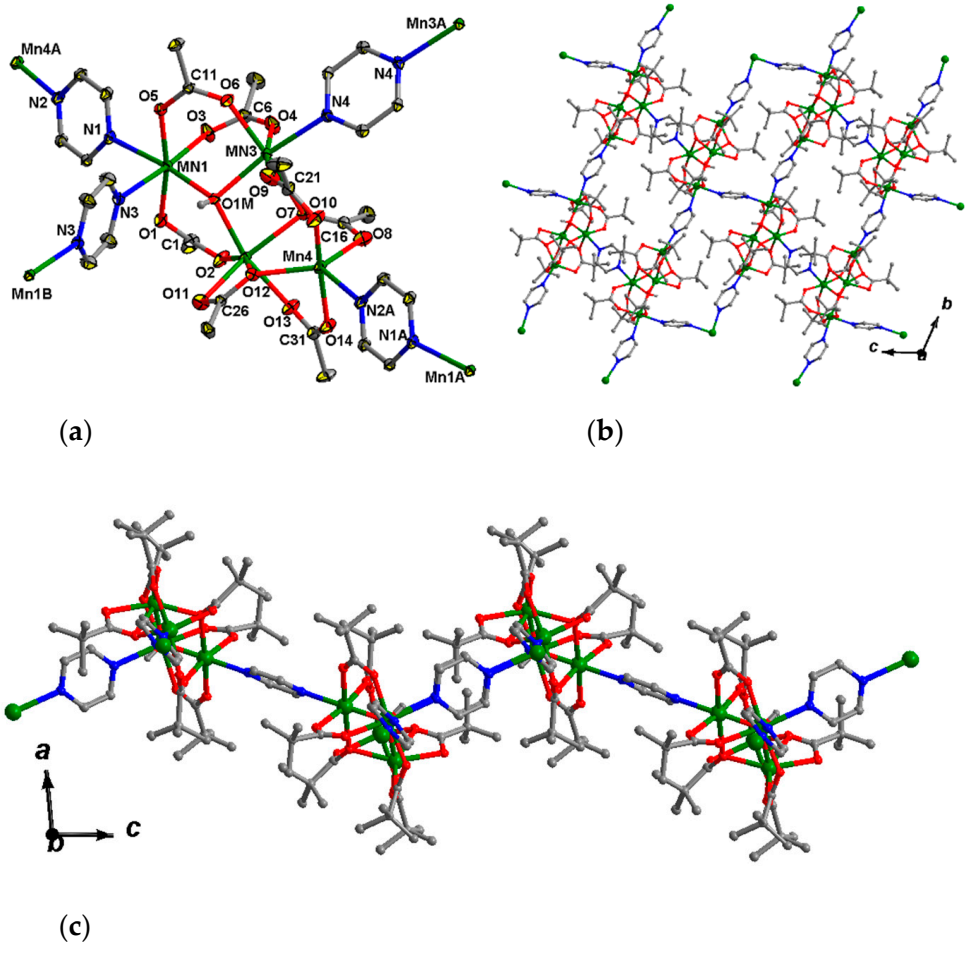

Figure 5. Fragment of crystal lattice (**a**) and 2D-grid (**b**,**c**) of **7**. H atoms at carbon atoms and methyl groups of pivalate ions (in **a**) are omitted for clarity, the displacement ellipsoids are drawn at the 30% probability level (in **a**).

Each Mn_4 unit is connected with other four Mn_4 units by four pyrazine bridges, while each pyrazine links two tetranuclear units. Such an arrangement results in the formation of a 2D polymer. The 2D-layers are parallel to the *bc* plane (Figure 5b,c).

2.2.6. Compound **8**

The complex **8** crystallizes in the monoclinic space group *C*2/*c* as a solvate with four molecules of MeCN. The molecule of **8** has axial symmetry, with axis 2 passing between the Fe1 and Fe1A atoms through the O1M, O2M, C21, C22, C26 and C27 atoms. The structure of the complex is similar to that of the known hexanuclear complexes $[Mn^{II}_4Mn^{III}_2(O)_2(O_2CR)_{10}(L)_4]$, where L is a neutral N- or O-donor ligans [71–73] but where the central atoms are Fe^{III} instead of Mn^{III}. The central Fe^{III} ions (Fe1 ... Fe1A 2.8824(10) Å) possess O_6 donor sets (Fe–O(μ_4-O) 1.953(2), 1.962(2) Å, Fe–O(Piv) 2.020(2)–2.070(2) Å), two terminal Mn^{II} ions (Mn ... Fe 3.1806(8)–3.5075(8) Å, Mn ... Mn 3.4831(11), 3.4841(11) Å) are located in O_5N donor sets (Mn–O(μ_4-O) 2.085(2) Å, Mn–O(Piv) 2.101(3)–2.492(2) Å, Mn-N 2.343(4), where N is an atom of a MeCN molecule, and two terminal Mn^{II} ions are located in O_6 donor sets (Mn–O(μ_4-O) 2.086(2) Å, Mn–O(Piv) 2.104(3)–2.522(2) Å, Mn–O(HPiv) 2.240(3) (Figure 6). H-bonds are formed between of a coordinated molecule of acid and the O atom of a bridging carboxylate group (O12 ... O4 2.603(4) Å, O12–H 0.84 Å, O4 ... H 1.77 Å, angle O12–H–O4 169°).

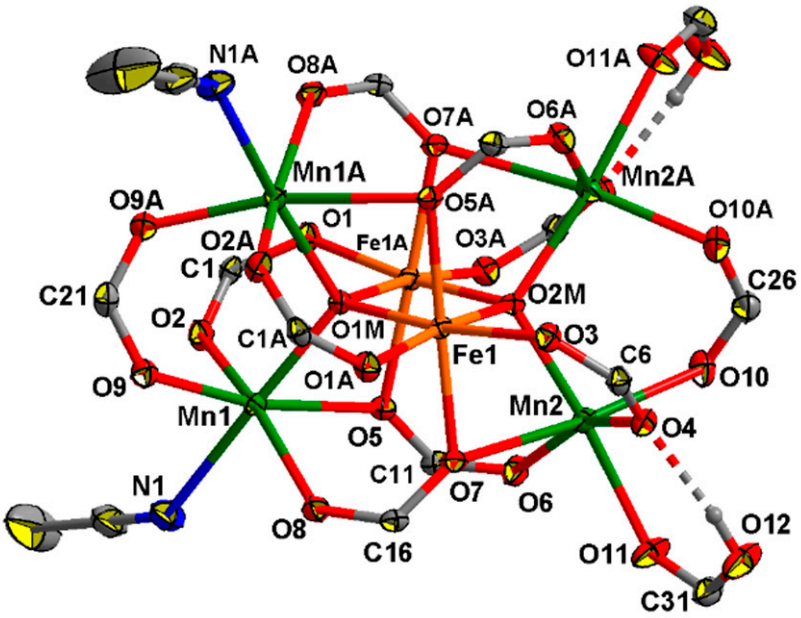

Figure 6. The structure of $[Mn_4Fe_2O_2(Piv)_{10}(MeCN)_2(HPiv)_2]$ in **8** (atoms with an additional character in the atom labels are at $(1 - x, y, 1/2 - z)$). H atoms at carbon atoms and methyl groups of pivalate ions are omitted for clarity, the displacement ellipsoids are drawn at the 30% probability level.

2.2.7. Compounds **9–11**

Coordination polymers **9–11** are built by linking a neutral trinuclear block, $\{Fe_2MnO(OAc)_6\}$, with neutral pyridine-containing bridges. The structure of the $\{Fe_2MnO(OAc)_6\}$ unit in all these complexes is almost the same (such unit in compound **9** is shown on Figure 7 as example). In this block three metal ions (two Fe^{III} and Mn^{II}) are located in the corners of an irregular triangle and generally cannot be distinguished by X-ray crystallography, so the assignment of metal ions was arbitrary. These metal ions are linked by μ_3-O atoms and six bridging acetates, so oxygen donors occupy five positions in the coordination sphere of each metal ion. The sixth positions are taken up by a donor atom (N or O) from other ligands (4,4′-bipy, bpe or DMF), so that each metal ion is located in a distorted octahedral donor set.

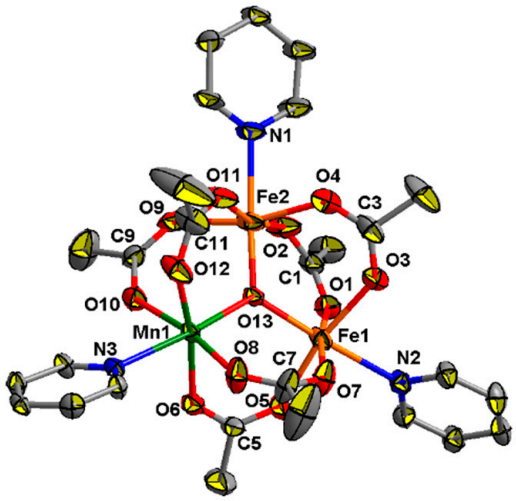

Figure 7. The structure of $\{MnFe_2O(OAc)_6(C_5H_4N)_3\}$ fragment in **10**. All hydrogen atoms are omitted for clarity. Only one pyridine ring from each 4,4′-bipy ligand is shown.

M—M separations within trinuclear acetates in compounds **9**–**11** fall in range 3.240(2)–3.353(2) Å. M–(μ_3-O) bond lengths lie in the range from 1.837(6) to 2.056(7) Å, M–O(carboxylate) bonds vary between 2.011(6) to 2.155(8) Å, which is typical for μ_3-oxocentered carboxylates [30].

In the crystal lattice of **9** trinuclear μ_3-oxocentered units $\{MnFe_2O(OAc)_6\}$ are connected by 4,4′-bipy molecules. 3/4 of trinuclear blocks are linked by 4,4′-bipy with formation of a 1D zig-zag chain. Two metal ions from each Fe_2Mn unit take part in such chain formation, while the third metal ion is bound to a non-bridging 4,4′-bipy molecule or a "terminal block" $\{MnFe_2O(OAc)_6(4,4'\text{-bipy})_3\}$. Thus, there are three types of trinuclear $MnFe_2$ blocks in **9** (Figure 8):

(1) $MnFe_2$ units in 1D chains, bound to two bridging 4,4′-bipy and one additional non-bridging 4,4′-bipy (type A);
(2) $MnFe_2$ units in $\{MnFe_2O(OAc)_6(4,4'\text{-bipy})_3\}$ residues (type B);
(3) $MnFe_2$ unit in 1D chains, bound to two bridging 4,4′-bipy and one type B unit (type C).

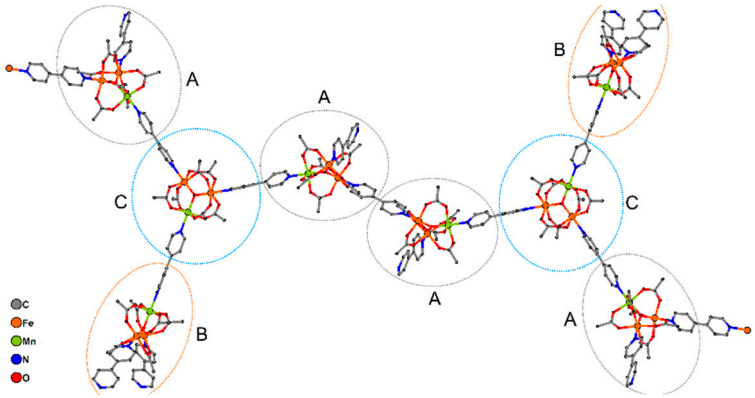

Figure 8. A fragment of 1D chain of **9**. Hydrogen atoms and solvent are omitted for clarity. Note that one bipy molecule in Fragment A is non-bridging; no coordinated metal ions was deleted for fragment A on the figure.

The distance between μ_3-O atoms of neighboring Fe_2Mn blocks in one 1D chain in **9** is equal to 15.222(8) Å in the case of AA blocks, 15.323 Å for AC blocks and 15.49(1) Å for BC blocks, while the angles between lines connecting the μ_3-O atoms of the neighboring trinuclear blocks, are close to 120° (from 116.83(4)° to 120.99(2)°). Torsion angles between

lines connecting four μ_3-O atoms of adjacent Fe_2Mn blocks, are equal to 180 ° for a CAAC fragment (i.e., all μ_3-O atoms for this fragment belong to one plane) and ±119.64(5)° for ACAA and AACA fragments. In other words, one 1D chain of **9** turns clockwise twice by 119.64(5)°, as implied by the torsion angles for ACAA or AACA, then all μ_3-O atoms lie in one plane in the CAAC fragment and finally the chain turns twice counterclockwise by 119.64(5)° in the ACAA and AACA fragments. The main axes of chains in compound **9** are directed along the (c-$\frac{1}{2}a$) vector (Figure 9).

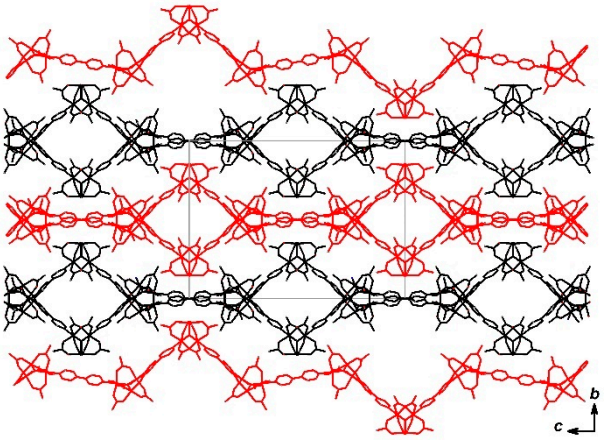

(**a**)

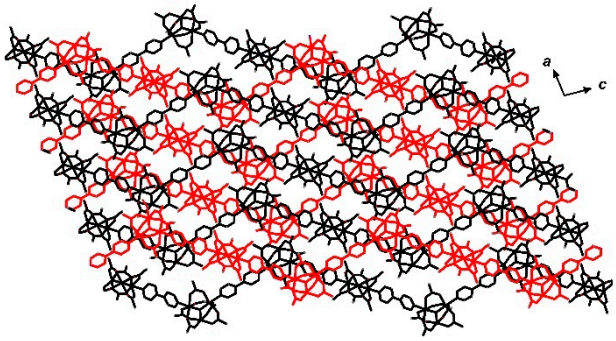

(**b**)

Figure 9. Fragment of crystal structure of **9**. View along crystallographic axes a (**a**) and b (**b**). All non-bridging bipy molecules, terminal $Fe_2MnO(OAc)_6(4,4'\text{-bipy})_3$ blocks, hydrogen atoms and non-coordinated DMF molecules are omitted for clarity.

The twofold axis passes through μ_3-O atoms of trinuclear blocks B and C. Also the local inversion centers are located between the pyridine groups of 4,4′-bipy molecules which bind two A type trinuclear blocks. The crystal lattice of **9** does not contain continuous channels (see Figure S2, Supporting Information).

2.2.8. Complexes **10** and **11**

These are built from trinuclear units $\{Fe_2MnO(OAc)_6\}$ bound by bpe molecules (Figure 10a). Two metal ions in each trinuclear block coordinate with pyridine rings from bridging bpe, leading to 1D-chain formation. The third metal ion is bound to a nitrogen atom of a terminal (non-bridging) bpe in **10** or oxygen atom of coordinated DMF in **11** (Figure 10b).

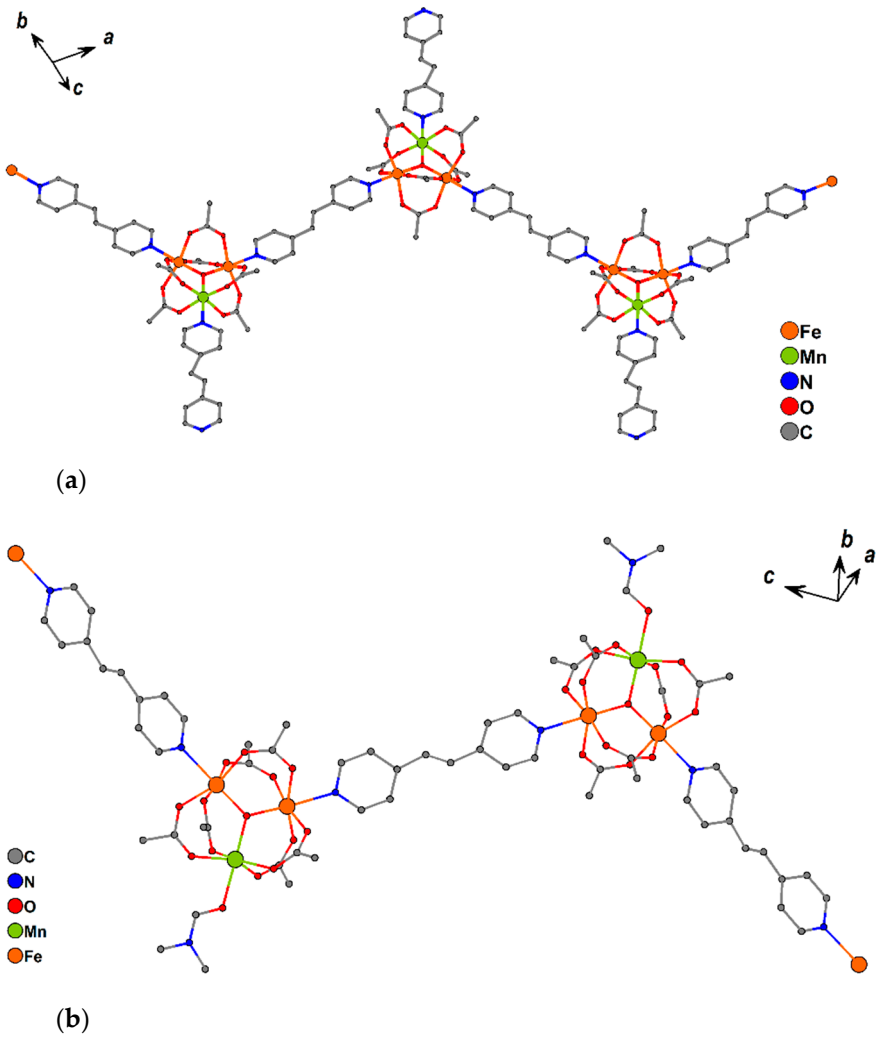

Figure 10. Fragments of 1D chains of **10** (**a**) and **11** (**b**). Hydrogen atoms and non-coordinated solvent molecules are omitted for clarity.

Chains of compound **10** are parallel and directed along the a-$\frac{1}{2}b$ vector. The non-coordinated pyridine ring of bpe in one chain and the pyridine ring of a bridging bpe ligand from the neighboring chain are almost parallel (the angle between mean planes of these rings is 4.1(5)°), and the closest distance between these rings is 3.38(2) Å (the distance between centroids of the rings is 3.634(6) Å), the slippage is 1.179 Å, which can allow for π-interactions (Figure 11a).

Chains of compound **11** are also parallel and directed along the c vector (Figure 11). No specific interactions between different chains are found. Due to this peculiarities of the chain packing channels of dimensions 5 × 12 Å directed along the a axis form in the crystal lattice (Figure 12). Estimation of solvent-accessible volume, performed by PLATON software [76], gives a value of 36% for **11**, containing DMF molecules coordinated to metal ions, or 45% for a structure, if coordinated DMF is removed assuming that such removal does not lead to crystal lattice collapse (calculated for a probe molecule with r = 1.4 Å). These values correspond to ca. 0.32 $cm^3\ g^{-1}$ pore volume, occupied by solvent in **11**, assuming that the volume occupied by coordinated DMF is not included in this value, or 0.40 $cm^3\ g^{-1}$, if the volume of coordinated DMF is included.

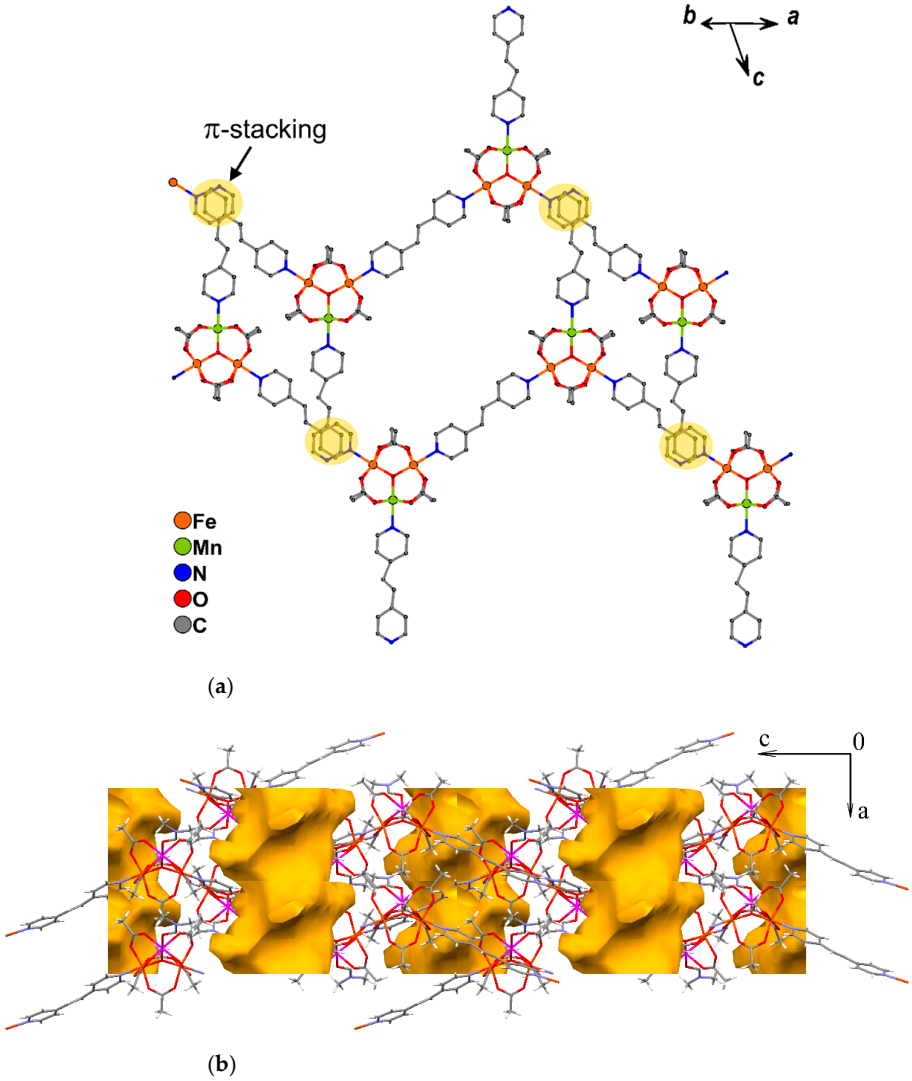

Figure 11. π-stacking interactions between the neighboring chains of **10** (**a**) and 1D-channels in crystal lattice of **11(-DMF)** (**b**). Hydrogen atoms and solvent molecules are omitted for clarity.

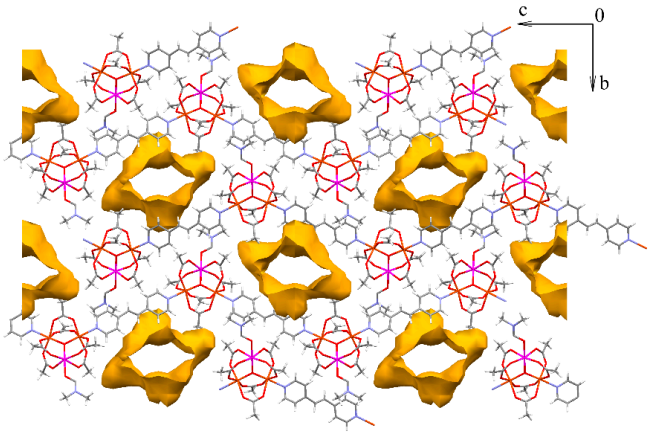

Figure 12. Channels in crystal lattice of **11**·3DMF (projection along *a* axis). Solvent molecules (including coordinated DMF) and hydrogen atoms are omitted for clarity.

2.3. Thermal Stability and Sorption Properties of 11·3.5DMF

The thermal stability of **11**·3.5DMF was studied by thermogravimetry. Upon heating to 275 °C, compound **11**·3.5DMF lost 26% of its weight, which corresponds to the release of both non-coordinated and coordinated solvent (Figure 13). An abrupt weight loss began at 275 °C, which was completed at 400 °C and could be associated with decomposition of the compound. The total weight loss was equal to 76.6% and corresponded to the formation of $Fe_2O_3 \cdot 1/3Mn_3O_4$ (Figure 13a). Loss of solvent and coordinated DMF led to significant lattice disorder, as it can be concluded by comparison of the powder XRD pattern of vacuum-dried product at 145 °C and the powder XRD pattern, calculated from the single-crystal structure (Figure 13b).

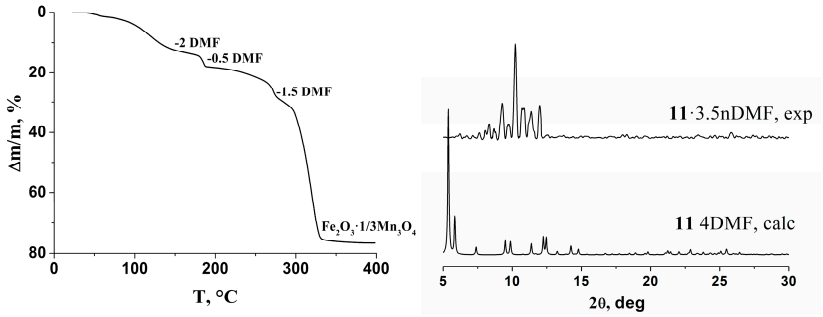

(**a**) (**b**)

Figure 13. TG curve for compound **11**·3.5DMF (**a**) and powder XRD patterns for vacuum-dried at 145 °C sample of **11**·3.5DMF and calculated from single-crystal X-ray data for **11** (**b**).

For sorption experiments compound **11**·3.5DMF was heated in vacuum at 153 °C during 6 h, which led to removal of non-coordinated and coordinated DMF. The desolvated sample is hereinafter referred to as **11′**.

Compound **11′** showed only surface sorption of N_2 or H_2 at 78 K, which is evidence of crystal lattice collapse and is consistent with the powder XRD data. In contrast, **11′** absorbed significant quantities of methanol and ethanol at 298 K (Figure 14). Such a difference between absorption of gases and alcohols can be caused by expansion of crystal lattice of **11′** upon interaction with methanol and ethanol, similarly to reported gate-opening phenomena [77] and previously reported cases of alcohol absorption by coordination polymers [18]. Both in the cases of methanol and ethanol, the sorption capacity gradually increased to ca. 0.42 $cm^3 \cdot g^{-1}$ (methanol) or 0.35 $cm^3 \cdot g^{-1}$ (ethanol), which is in good agreement with the value of solvent-accessible volume estimated from the crystallographic data (vide supra).

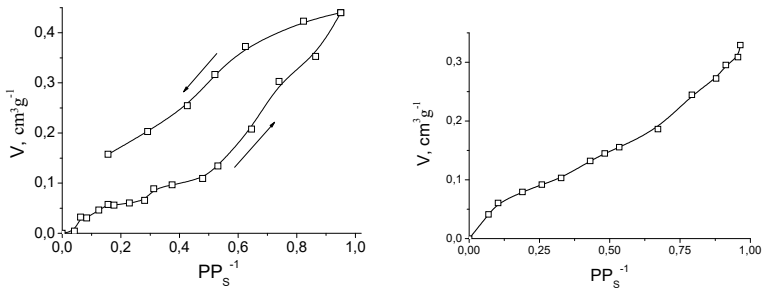

(**a**) (**b**)

Figure 14. Sorption isotherms of methanol (**a**) and ethanol (**b**) by **11′** at 293 K. Arrows on Figure (**a**) indicate directions of absorption and desorption.

The plateau in the methanol absorption isotherm at PP_S^{-1} ca. 0.07–0.3 ($V_{abs.}$ about 0.05 $cm^3\ g^{-1}$) corresponds to a methanol to Fe_2Mn molar ratio 1:1 and can be associated with methanol coordination to the metal ion (in a position which was occupied by coordinated DMF in **11**). It can be concluded from the presence of such a plateau that there is a noticeable difference between the energy of methanol coordination to a metal ion in **11′** and the energy of further methanol interaction with **11′**·CH_3OH. In contrast, a similar plateau was not found in the ethanol absorption isotherm: ethanol binding by **11′** after filling of unsaturated metal sites seems to be as efficient as ethanol binding due to its coordination (which most probably does occur). Anyhow, the maximal achieved sorption capacity of **11′** corresponds to ca. 10.5 moles of methanol or ca. 5 moles of ethanol per 1 mole of Fe_2Mn, which is significantly higher than the sorption capacity associated with coordination.

2.4. EPR Spectroscopy

X-band EPR experiments for polycrystalline samples **1** and **2** were performed at 293 K. The spectra of **1** and **2** show an intense singlet without hyperfine structure with $g \approx 2.00$. In the low magnetic field lines of low intensity are observed; their origin can be explained by the exchange interactions between paramagnetic manganese ions (Figure 15).

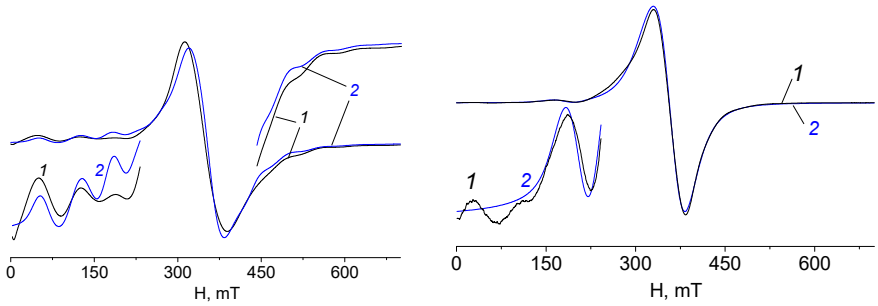

(**a**) (**b**)

Figure 15. EPR spectra of polycrystalline samples of **1** (**a**) and **2** (**b**) at 293 K (1—experimental, 2—calculated).

Since antiferromagnetic interactions with $J = -1.03\ cm^{-1}$ were found in **1** and **2** by magnetic data analysis (see below), all possible magnetic states of dimer of two Mn^{2+} ions with spins $S_{1,2} = 5/2$, notably, S = 0, 1, 2, 3, 4, 5 ($S = S_1 + S_2$) were equally populated. Furthermore, since $|J| > h\nu \approx 0.3\ cm^{-1}$, transitions between states with different total spin S can be neglected. Thus, the spin Hamiltonian for **1** and **2** is the sum of spin Hamiltonians of five dimers with different total spins. The spin Hamiltonian (1) for single ion in **1** or **2** has a rhombic symmetry:

$$\hat{H}_i = g_{iz}\beta H_z S_{iz} + g_{ix}\beta H_x S_{ix} + g_{iy}\beta H_y S_{iy} + d_i \cdot (S_{iz}^2 - \frac{1}{3}S_i(S_i+1)) + e_i \cdot (S_{ix}^2 - S_{iy}^2), \quad (1)$$

where g_{iz}, g_{ix}, g_{iy}—z, x, y—g-tensor components of monomer i, where $i = 1, 2$; S_{iz}, S_{ix}, S_{iy}–projections of spin operator of monomer on coordinate axes, $S_i = 5/2$; d_i, e_i—component of fine interaction tensor (so-called, single-ion). Mn^{2+} ion has half-filled d^5 shell and S-state, so g-tensor is isotropic and close to spin-only value, so, $g_{iz} = g_{ix} = g_{iy} = g = 2.0023$.

Spin Hamiltonian (2) of dimer is the sum of two Hamiltonians for interactions within mononuclear fragments of molecule and the part of their interaction:

$$\begin{gathered}\hat{H} = \hat{H}_1 + \hat{H}_2 - 2JS_1S_2 + d_{12} \cdot (S_{1z} \cdot S_{2z} - \tfrac{1}{3}S_1 \cdot S_2) + \\ e_{12} \cdot (S_{1x} \cdot S_{2x} - S_{1y} \cdot S_{2y})\end{gathered} \quad (2)$$

where d_{12}, e_{12} are the components of fine interaction tensor, caused by dipole interaction of manganese ions.

For the total spin of dimer and neglecting of transitions between multiplets with different total spin $S = S_1 + S_2$, spin Hamiltonian (3) can be used:

$$\begin{array}{c} \hat{H}_S = g\beta(H_z S_z + H_x S_x + H_y S_y) + D_S \cdot (S_z^2 - \frac{1}{3}S(S+1)) + E_S \cdot (S_x^2 - S_y^2) \\ -2J(S(S+1) - S_1(S_1+1) - S_2(S_2+1)) \end{array} \quad (3)$$

where D and E are the components of fine interaction tensor, associated with parameters $d_{1,2}$, $e_{1,2}$, d_{12} ue_{12} by the following formula [78]:

$$D_S = \alpha_S d_{12} + \beta_S d_1 \qquad E_S = \alpha_S e_{12} + \beta_S e_1$$

$$\alpha_S = \frac{S(S+1) + 4S_1(S_1+1)}{2(2S-1)(2S+3)} \qquad \beta_S = \frac{3S(S+1) - 3 - 4S_1(S_1+1)}{(2S-1)(2S+3)} \quad (4)$$

The spin Hamiltonian (3) was diagonalized numerically. Calculations of resonance fields of spin Hamiltonian (3) required to build a theoretical spectrum were carried out by the Belford method [79], which involves finding the values of magnetic field H, for which two eigenvalues of spin Hamiltonian (3) matrix, corresponding to two different eigenvectors, would differ on the $h\nu$.

The spin Hamiltonian parameters for compounds **1** and **2** are given in Table 1. Thus, while isotropic exchange of two dimers is same, fine interaction tensor causes a noticeable difference in the EPR spectra.

Table 1. Spin Hamiltonian parameters for **1** and **2**.

Compound	G	d_1 (cm^{-1})	e_1 (cm^{-1})	d_{12} (cm^{-1})	e_{12} (cm^{-1})
1	2.0023	0.00098	0.0105	0.0038	0.0067
2	2.0023	0.0368	0.0063	0.0347	0.0074

2.5. Magnetic Properties of Complexes **1, 2, 7**·*2MeCN and* **11**·*3.5DMF*

Magnetic properties of the representative complexes from the prepared series—compounds **1**, **2**, **7**·2MeCN and **11** 3.5DMF—were characterized by their temperature dependence of the molar magnetic susceptibility, χ_M.

2.5.1. Magnetic Properties of Complexes **1** and **2**

For both compounds $\chi_M T$ values (here and below χ_M is the magnetic susceptibility per formula unit and T is the temperature in K) monotonously decrease upon lowering the temperature from 8.17 (for **1**) or 8.64 (for **2**) $cm^3 \cdot K \cdot mole^{-1}$ at 300 K to 7.81 (for **1** at 60 K) or 7.74 (for **2** at 68 K) $cm^3 \cdot K \cdot mole^{-1}$, after which it falls sharply to 4.01 (for **1** at 5 K) or 0.82 (for **2** at 2 K) $cm^3 \cdot K \cdot mole^{-1}$. Room-temperature values of $\chi_M T$ are close to the expected spin-only value (8.75 $cm^3 \cdot K \cdot mole^{-1}$ for a system with two non interacting magnetic centers with $S = 5/2$).

The spin Hamiltonian for dinuclear blocks Mn_2 in **1** and **2** is shown as Equation (5).

$$\hat{H} = -2J_{Mn-Mn}\hat{S}_1\hat{S}_2 + \beta H g_{Mn}(\hat{S}_1 + \hat{S}_2) \quad (5)$$

where the first summand corresponds to the superexchange interactions between Heisenberg spins localized at metal sites ($J_{Mn\text{-}Mn}$), and the second summand corresponds to the isotropic interactions between local spins and the external field through Zeeman interactions [80].

It should be noted that the spin-Hamiltonian proposed for interpretation of the magnetic properties differed from the one employed for interpretation of the EPR spectra of the same compounds. There was no contradiction between these Hamiltonians, as both of them were "partial" variations of the complete spin-Hamiltonian describing the system of the unpaired electron within the species of the compounds. This complete spin-Hamiltonian had to include all the terms: (i) Zeeman interactions with the external magnetic field; (ii)

exchange interactions between the ions; (iii) zero-field splitting. However, the variations of exchange interaction parameters could not notably influence the studied EPR spectra (*vide supra*), while the influence of zero-field splitting on the magnetization curves was negligible compared to the influence of the exchange interactions. Thus, introduction of the corresponding terms into the spin-Hamiltonians and efforts to extract the corresponding parameters from the data simulations would not produce any reliable values. Regarding Zeeman interactions, their principal parameters—g-factors—were consistent (within accuracy of the methods) for the EPR and magnetochemical data.

Temperature-independent paramagnetism (*tip*) term was also introduced. Intermolecular interactions were taken into account within molecular field model (zJ' term).

Analytical expression for the $\chi_M T$ values for the Mn_2 unit [80] is the following:

$$\chi_M T = \frac{2Ng^2\mu_B^2}{k} \cdot \frac{e^x + 5e^{3x} + 14e^{6x} + 30e^{10x} + 55e^{15x}}{1 + 3e^x + 5e^{3x} + 7e^{6x} + 9e^{10x} + 11e^{15x}}, \quad (6)$$

where $x = -J/kT$.

The best agreement between experimental and calculated $\chi_M T$ curves (Figure 16) was achieved at parameters $J_{Mn\text{-}Mn}$ = −1.03(2) cm^{-1}, g_{Mn} = 2.0, zJ' = −0.19(1) cm^{-1} ($R^2 = 2.44 \cdot 10^{-5}$) for compound **1** and $J_{Mn\text{-}Mn}$ = −1.03(2) cm^{-1}; g_{Mn} = 2.0, *tip* = $7 \cdot 10^{-4}$ ($R^2 = 9.87 \cdot 10^{-5}$) for compound **2** (where $R^2 = \sum[(\chi_M T)_{obs.} - (\chi_M T)_{calc.}]^2/(\sum(\chi_M T)_{obs.}{}^2)$).

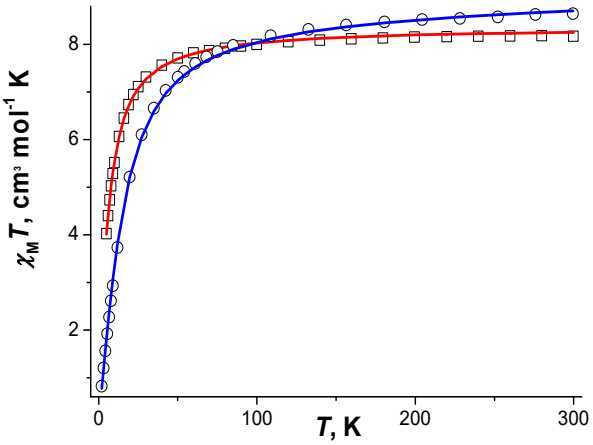

Figure 16. $\chi_M T$ vs. T dependencies and the calculated curves (–) for **1** (ϒ), **2** (⊄).

Absolute values of $J_{Mn\text{-}Mn}$ for **1** and **2** are higher than those reported for benzoato- and phtalato-bridged dinuclear blocks $Mn_2(\mu\text{-}O_2C)_2(\eta\text{-}O_2C)_2$ [81,82], which is consistent with the higher electron-donating ability of the *tert*-butyl groups in pivalates compared to phenyl group.

2.5.2. Magnetic Properties of Complex **7** ·2MeCN

For the compound **7** 2MeCN the $\chi_M T$ value monotonically decreases upon lowering the temperature from 15.78 $cm^3 \cdot K \cdot mole^{-1}$ at 300 K to 0.53 $cm^3 \cdot K \cdot mole^{-1}$ at 3 K. The room-temperature value of $\chi_M T$ is lower than the expected spin-only value (17.5 $cm^3 \cdot K \cdot mole^{-1}$ for a system with four non-interacting magnetic centers with $S = 5/2$). The coupling scheme within a tetranuclear unit is presented in Figure 17. The spin Hamiltonian for tetranuclear block Mn_4 takes the form:

$$H = -2J_1 S_{Mn1} \cdot S_{Mn3} - 2J_2 S_{Mn1} S_{Mn2} - 2J_3 S_{Mn2} \cdot S_{Mn3} - 2J_4 S_{Mn3} S_{Mn4} \\ -2J_5 S_{Mn2} S_{Mn4} + g_{Mn}\beta(S_{Mn1} + S_{Mn2} + S_{Mn3} + S_{Mn4} + S_{Mn5}) \cdot H \quad (7)$$

where the first five summands correspond to the superexchange interactions between Heisenberg spins localized at metal sites (J_1–J_5), and the last summand corresponds to

the isotropic interactions between local spins and the external field through Zeeman interactions (g_{Mn}), respectively [80]. A temperature-independent paramagnetism (tip) term was also introduced.

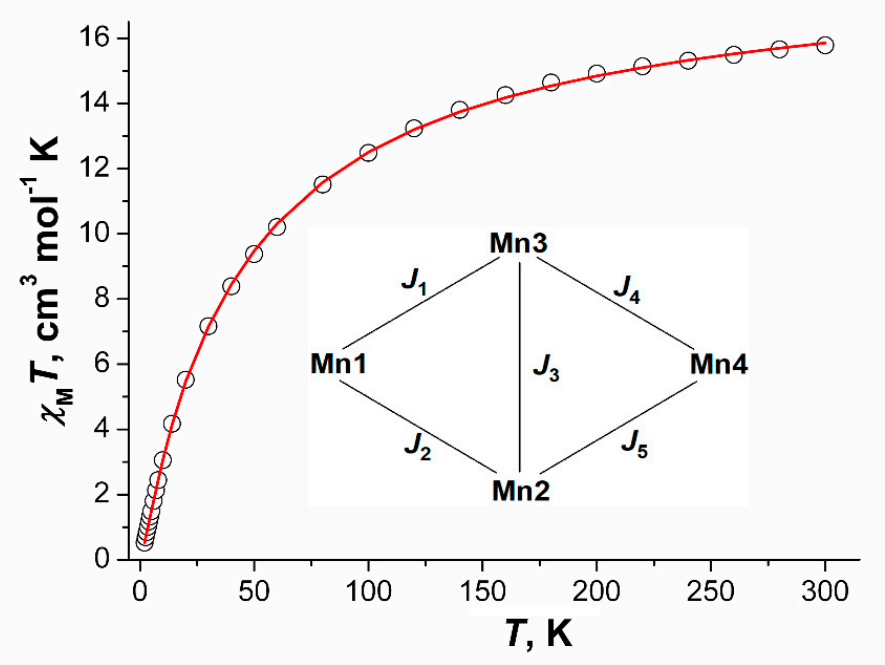

Figure 17. $\chi_M T$ vs. T dependence, the calculated curve (–) and coupling scheme within a tetranuclear unit Mn_4 for compound **7** 2MeCN.

Calculation of the exchange coupling parameters were performed by full-matrix diagonalization using the Mjöllnir software [16,83]. Uncertainty values of simulation parameters were estimated as described previously [33]. Briefly, digits in brackets indicated deviation of the value, which caused 10% increase of R^2.

The best correspondence between experimental and calculated $\chi_M T$ values for compound **7** was achieved for the parameters $J_1 = -2.69(2)$ cm^{-1}, $J_2 = -2.38(2)$ cm^{-1}, $J_3 = -0.8(1)$ cm^{-1}, $J_4 = -0.42(2)$ cm^{-1}, $J_5 = -0.8(2)$ cm^{-1}, $g_{Mn} = 2.0023$ (fixed), $zJ' = -0.5(1)$ cm^{-1}, $tip = 0.00129$ ($R^2 = 2.3 \cdot 10^{-5}$).

Exchange coupling parameters have larger values for magnetic interactions of Mn1 ion with Mn2 and Mn3 which agree with the structural data: the Mn1 ion has in its coordination sphere two N atoms from two pyrazine molecules which increase its electron density and amplify the antiferromagnetic interactions. Additionally, the most effective way of magnetic interactions transfer through the OH group in the trinuclear Mn1Mn2Mn3 unit which also agrees with the received data.

The Mn_4 units can be selected in the 2D-coordination polymer $[Mn_4(\mu_3\text{-OH})(Piv)_7(\mu\text{-pz})_2]_n$, and exchange coupling within these units can be presented by five integrals J_1–J_5 (Figure 17). From the experimental $\chi_M T$ vs. T curve the following values could be calculated by full-matrix diagonalization (performed using the Mjöllnir software [16,83]) (cm^{-1}): $J_1 = -2.7$, $J_2 = -2.4$, $J_3 = -0.8$, $J_4 = -0.4$, $J_5 = -0.8$. Signs and magnitudes of these J were estimated using broken-symmetry DFT calculations with TPSSh functional and LANLTZ ECPs (3d ions)/def2-SVP basis set. For calculation of each J value all Mn^{2+} ions in the Mn_4 core except the two ions taking part in the coupling were "substituted" by diamagnetic Zn^{2+} ions, and then calculations of the high-spin (HS) and the broken symmetry (BS) states' energies (see Experimental part for details of their construction) were performed. The results evidence that two exchange integrals, J_1 and J_2, have the same order of magnitude (-6.9 and -6.4 cm^{-1}, respectively); while J_3, J_4, J_5 fall in the range from -0.9 to -1.2 cm^{-1}. The exchange through pz bridge is estimated as -0.2 cm^{-1}. These results correlate with J

values, found from χ_MT vs. T curve simulation ($|J_1|$, $|J_2|$ the highest and close to each other, $|J_3|$–$|J_5|$—lower and close to each other).

It should be noted that fitting of the $\chi_M T$ vs. T curve for **7** 2MeCN could be fitted with simpler Hamiltonian (8):

$$\hat{H} = -2J_1(S_1S_2 + S_3S_4) - 2J_2\ S_2S_3 \quad (8)$$

with $J_1 = -2.08 \pm 0.02$ cm^{-1}, $J_2 = -3.92 \pm 0.07$ cm^{-1}, $g = 2$ (fixed), however there are no reasons to neglect interactions between other Mn^{II} ions, since structural features of the bridges between them are similar. The $\chi_M T$ vs. T curve calculated with these parameters is visually the same as shown on Figure 17.

2.5.3. Magnetic Properties of Complex 11·3.5DMF

For compound **11**·3.5DMF, the value of $\chi_M T$ at 300 K was 4.66 cm^3·K·mol^{-1}, which is significantly lower than the expected spin-only value for three non-interacting spins 5/2 (13.125 cm^3·K·mol^{-1}). On cooling, the $\chi_M T$ vs. T curve decreased monotonically to 3.20 cm^3·K/mol at 50 K, after which it sharply fell to 2.08 cm^3·K·mol^{-1} at 2 K.

The coupling scheme within a trinuclear unit is represented on Figure 18. The spin Hamiltonian for trinuclear blocks Fe_2Mn takes the form:

$$\begin{gathered} H = -2J_{Fe-Fe}S_{Fe_1} \cdot S_{Fe_2} - 2J_{Fe-Mn}(S_{Fe_1} + S_{Fe_2}) \cdot S_{Mn} + \\ + g_{Mn}\beta S_{Mn} \cdot H + g_{Fe}\beta(S_{Fe_1} + S_{Fe_2}) \cdot H \end{gathered} \quad (9)$$

where first line corresponds to the superexchange interactions between Heisenberg spins localized at metal sites ($J_{Fe\text{-}Fe}$ and $J_{Fe\text{-}Mn}$), the second line corresponds to the isotropic interactions between local spins and the external field through Zeeman interactions (g_{Fe} and g_{Mn}), respectively [80]. Intermolecular interactions were taken into account within molecular field model.

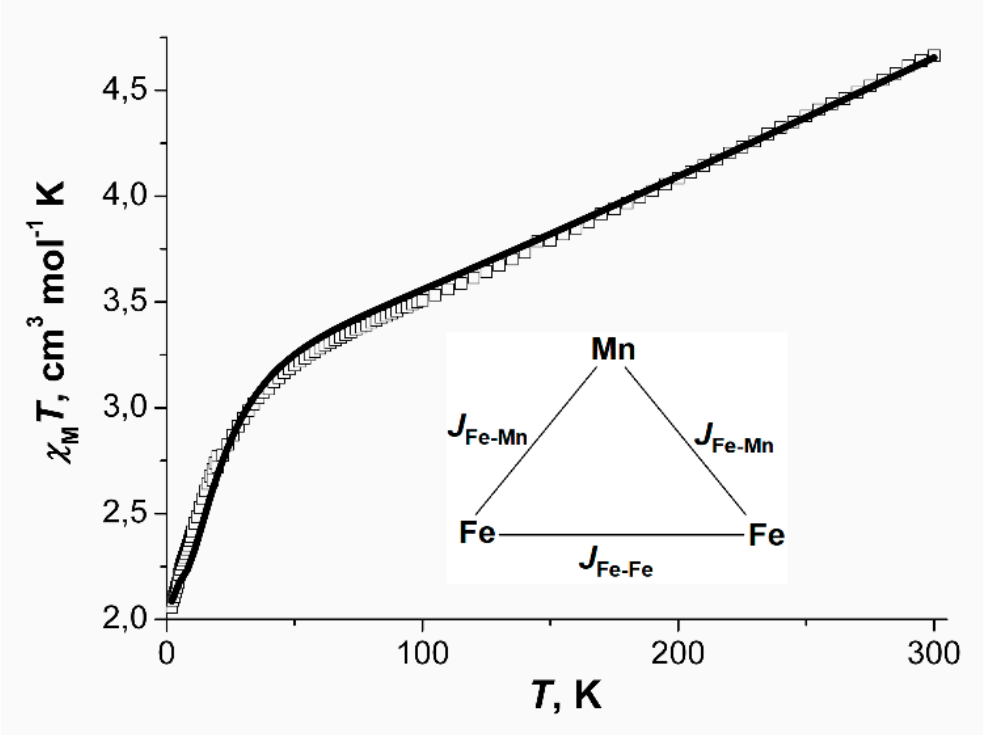

Figure 18. $\chi_M T$ vs. T dependence, the calculated curve (–) and coupling scheme within a trinuclear unit Fe_2Mn for compounds **11**·3.5DMF.

The best correspondence between experimental and calculated $\chi_M T$ values for the compound was achieved at parameters $J_{Fe\text{-}Fe}$ = −57.8(2) cm^{-1}, $J_{Fe\text{-}Mn}$ = −20.12(7) cm^{-1}, $g_{Fe} = g_{Mn}$ = 2.0023 (fixed), zJ' = −0.10(1) cm^{-1}, $\chi_{\text{impurities}}$ = 3.2% ($S_{\text{impurities}}$ = 5/2).

Absolute values of $J_{Fe\text{-}Mn}$ and $J_{Fe\text{-}Mn}$ for **11** 3.5DMF are higher than those reported for the trifluoroacetate complex [$Fe_2MnO(O_2CCF_3)_6(H_2O)_3$] ($J_{Fe\text{-}Fe}$ = −56.50(7) cm^{-1}, $J_{Fe\text{-}Mn}$ = −16.23(4) cm^{-1} [31], which is consistent with the higher electron-donating ability of the methyl group in acetate relative to CF_3-group. However, for {$Fe_2MnO(Piv)_6$} blocks exchange coupling parameters [58] have close values to exchange coupling parameters for **11**·3.5DMF. It can be explained by different nitrogen ligands: pyridine group in **11**·3.5DMF in comparison with hexamethylenetetramine [58] compensates lower electron donor efficiency of acetate group in comparison with pivalate group [84].

3. Experimental

3.1. Materials and Methods

Reagents and solvents were commercially available (Sigma-Aldrich, Aldrich, St. Louis, MO, USA) and were used without further purification. Manganese pivalate [$Mn(Piv)_2(EtOH)]_n$ and trinuclear acetate [$MnFe_2O(OAc)_6(H_2O)_3$], used as starting compound, were prepared as previously reported [30,51]. C,H,N-analyses were performed using a 1106 instrument (Carlo Erba, Instruments, Egelsbach, Germany). IR-spectra were measured in KBr pellets on a Spectrum BX FT-IR spectrometer (Perkin Elmer, Waltham, MA, USA) in 400–4000 cm^{-1} range. The X-ray powder diffraction analysis of **6** was carried out on a G670 (HUBER, Offenburg, Germany) Guinier camera using $CuK_{\alpha 1}$ radiation on air. The X-ray powder diffraction analysis of **11** was performed on a D8 Advance instrument (Bruker, Billerica, MA, USA) in air.

Thermogravimetric analyses (TGA) were performed in air on Q1500 instrument, (*Paulik-Paulik-Erdey*, Budapest, Hungary). The heating rate was 5 °C per minute. Sorption of methanol and ethanol by [$MnFe_2O(OAc)_6$(dpe)] was studied gravimetrically, using a tungsten microbalance at 293 K. Each point on the absorption and desorption isotherms corresponds to equilibrium conditions (no change of sample weight at certain $p \cdot {p_S}^{-1}$, where p_S is the pressure of saturated vapor of the compound at 293 K). This sample was thermally activated at 150 °C in vacuum at 10^{-2} Torr. Volume of pores was estimated from the quantity of adsorbed alcohol using its density in liquid phase at 293 K.

Magnetic measurements were performed on a MPMS-XL (for **11**), MPMS-5S (for **7**) and PPMS (for **1** and **2**) SQUID magnetometers (Quantum Design, San Diego, CA, USA) and intrinsic diamagnetic corrections were calculated using Pascal's constants [80]. The X-band EPR spectra for **1** and **2** were measured on a Bruker Elexsys E680-X spectrometer at T = 293 K.

3.2. Synthesis

3.2.1. Synthesis of [$Mn_2(Piv)_4$(2,2′-bipy)$_2$] (**1**) and [$Mn_2(Piv)_4(phen)_2$] (**2**)

The syntheses were carried out under an argon atmosphere. [$Mn(Piv)_2(EtOH)]_n$ (0.150 g, 0.50 mmol) was dissolved in MeCN (30 mL for **1** or 25 mL for **2**), followed by the addition of 2,2′-bipyridine (0.078 g, 0.50 mmol) for **1** or 1,10-phenantroline (0.090 g, 0.50 mmol) for **2**. The resulting colorless solution was heated at 80 °C during 30 min, then concentrated to 6–8 mL for **1** or 4–6 mL for **2** and kept at 5 °C during 24 h. Crystals were isolated by decantation, washed by cold MeCN and dried under argon stream. Yield of **1**: 0.14 g (67%), yellow crystals; **2**: 0.162 g (74%), colorless crystals. Anal, calc. for **1**, $C_{40}H_{52}Mn_2N_4O_8$/found, %: C 58.1/58.0, H 6.3/6.5, N 6.8/6.9. IR-spectrum of **1** (cm^{-1}): 3434 m, 3058 w, 2955 s, 2923 m, 2865 w, 1597 vs, 1542 s, 1516 s, 1482 s, 1420 s, 1373 m, 1359 m, 1225 m, 1143 w, 1101 w, 894 w, 864 w, 846 m, 792 b.w, 729 s, 637 w, 601 w. Anal, calc. for **2**, $C_{44}H_{52}Mn_2N_4O_8$/found, %: C 60.4/59.8, H 6.0/6.2, N 6.4/6.4. IR-spectrum of **2** (cm^{-1}): 3434 s, 2956 s, 2923 m, 2866 w, 1586 v.s, 1547 s, 1482 s, 1440 s, 1419 s, 1372 m, 1358 m, 1314 w, 1226 m, 1172 w, 1155 w, 1059 w, 1015 m, 893 m, 805 w, 792 w, 767 s, 738 m, 646 w, 625 w, 603 w, 558 w, 415 m.

3.2.2. Synthesis of $[Mn_4O_2(Piv)_6(2,2'\text{-bipy})_2]\cdot$MeCN (3·MeCN) (**3**) and $[Mn_4O_2(Piv)_6(phen)_2]\cdot$ 0.5MeCN (4·0.5MeCN) (**4**)

The syntheses were carried out under an argon atmosphere. $[Mn(Piv)_2(EtOH)]_n$ (0.150 g, 0.50 mmol) was dissolved in 30 mL of MeCN followed by the addition of 2,2′-bipyridine (0.078 g, 0.50 mmol) for **3·MeCN** or 1,10-phenantroline (0.090 g, 0.50 mmol) for **4·0.5MeCN**. The colorless solution was heated at 80 °C during 30 min, then kept under air at room temperature during 24 h for **3·MeCN** or 10 days for **4·0.5MeCN**. The precipitate was isolated by decantation and dissolved in 30 mL of THF, filtered and then kept under air at room temperature during one week. Brown crystals were isolated by decantation, washed by cold MeCN and dried on air. Yield of **3·MeCN**: 0.051 g (35%), brown microcrystals; yield of **4·0.5MeCN**: 0.045 g (29%), dark-brown crystals. Anal, calc. for **3·MeCN**, $C_{50}H_{70}Mn_4N_4O_{14}$/found, %: C 51.3/51.1, H 6.0/6.2, N 4.8/4.9. IR-spectrum of **3·MeCN** (cm^{-1}): 3433 m, 2956 m, 2925 m, 2868 w, 1589 v.s., 1570 s, 1482 s, 1441 m, 1415 s, 1370 s, 1357 m, 1317 w, 1225 m, 1155 w, 1016 w, 890 w, 789 w, 766 m, 740 w, 640 b.m, 431 m, 410 m. Anal, calc. for **4·0.5MeCN**, $C_{55}H_{71.5}Mn_4N_{4.5}O_{14}$/found, %: C 53.3/53.4, H 5.8/5.9, N 5.1/5.2. IR-spectrum of **4·0.5MeCN** (cm^{-1}): 3435 w, 2956 s, 2924 m, 2868 m, 1590 s, 1560 s, 1514 s, 1482 s, 1456 m, 1411 s, 1371 s, 1358 s, 1261 w, 1226 s, 1141 w, 1101 m, 1028 w, 891 w, 864 m, 853 m, 790 m, 732 s, 656 s, 639 s, 616 s, 420 bm.

3.2.3. Synthesis of $[Mn_6(OH)_2(Piv)_{10}(pym)_4]$ (**5**) and Synthesis of $[Mn_6O_2(Piv)_{10}(pym)_2]_n$ (**6**)

Syntheses were carried out under an argon atmosphere. $[Mn(Piv)_2(EtOH)]_n$ (0.6 g, 1.98 mmol) was dissolved in 30 mL of EtOH, followed by the addition of pyrimidine (0.11 g, 1.40 mmol). The colorless solution was heated at 80 °C during 30 min. For the isolation of **5** the solution was concentrated to 2–3 mL and cooled at −18 °C during 24 h. For the isolation of **6** the solution was kept on air at room temperature during 24 h. The crystals were isolated by decantation, washed by cold MeCN and dried under argon stream. Yield of **5**: 0.12 g (22%) colorless crystals; yield of **6**: 0.43 g (85%), colorless crystals. Anal, calc. for **5**, $C_{66}H_{108}Mn_6N_8O_{22}$/found, %: C 46.8/46.7, H 6.4/6.2, N 6.6/6.8. IR-spectrum of **5** (cm^{-1}): 3419 b.m, 2960 s, 2928 s, 1676 s, 1587 b.s, 1484 s, 1640 s, 1422 s, 1362 s, 1227 s, 1169 w, 1077 w, 1030 w, 937 w, 895 m, 790 m, 716 m, 636 m, 601s, 559 m, 540 m, 415 m. Anal, calc. for **6**, $C_{58}H_{98}Mn_6N_4O_{22}$/found, %: C 45.4/45.5, H 6.4/6.2, N 3.7/3.8. IR-spectrum of **6** (cm^{-1}): 3434 b.m, 2958 m, 2926 w, 2870 w, 1582 v.s, 1569 s, 1482 s, 1467 w, 1417 v.s, 1374 s, 1359 s, 1228 s, 1163 w, 1076 w, 1029 w, 1003 w, 892 w, 795 w, 786 w, 715 w, 632 w, 612 m, 557 w, 437 w, 404 w.

3.2.4. Synthesis of $[Mn_4(OH)(Piv)_7(pz)_2]_n\cdot 2n$MeCN (**7**·2MeCN)

The synthesis was carried out under an argon atmosphere. $[Mn(Piv)_2(EtOH)]_n$ (0.1 g, 0.33 mmol) was dissolved in 20 mL of MeCN, then a solution containing pyrazine (0.03 g, 0.33 mmol) in 5 mL MeCN was added dropwise. The colorless solution was kept at 25 °C during 48 h. Yellow precipitate with crystals was isolated by decantation, washed by cold MeCN and dried under argon stream. Yield 0.08 g (82%). Anal, calc. for $C_{47}H_{78}Mn_4N_6O_{15}$/found, %: C 47.6/47.4, H 6.6/6.8, N 7.1/7.2. IR-spectra (cm^{-1}): 3432 b.m, 2959 s, 2928 m, 2870 w, 1589 v.s, 1569 v.s, 1483 v.s, 1458 m, 1422 s, 1374 s, 1360 s, 1227 s, 1135 w, 1047 m, 893 w, 791 m, 600 m, 564 w, 450 w, 409 m.

3.2.5. Synthesis of $[Mn_4Fe_2O_2(Piv)_{10}(MeCN)_2(HPiv)_2]\cdot$2MeCN (**8**·2MeCN)

The synthesis was carried out under an argon atmosphere. A reaction mixture of $[Mn(Piv)_2(EtOH)]_n$ (0.8 g, 2.64 mmol) and $FeCl_3$ (0.122 g, 0.75 mmol) in 100 mL MeCN was heated (80 °C) during 30 min to complete the dissolution of reagents. The brown solution obtained was concentrated to 50 mL and kept at room temperature during 6 h. The white and brown precipitates formed were separated from the solution. The solution was concentrated to 20 mL and kept at room temperature during 24 h. Brown crystals were isolated by decantation, washed by cold MeCN and dried under argon stream. Yield 0.16 g (15%). Anal, calc. for $C_{64}Fe_2H_{116}Mn_4O_{26}N_2$ (without solvent molecules)/found,

%: C 46.3/46.4, H 7.0/6.9, N 1.7/1.6, Fe 6.7/6.6; Mn 13.2/13.0. IR-spectra (cm^{-1}): 3192 w, 2962 s, 2930 s, 2873 m, 1692 m, 1570 s, 1484 s, 1460 m, 1420 s, 1376 s, 1360 s, 1314 w, 1227 s, 1206 m, 1031 w, 938 w, 895 m, 872 w, 787 m, 764 v.w, 604 m, 574 m, 516 m, 420 s.

3.2.6. Synthesis of $[MnFe_2O(OAc)_6(4,4'\text{-bipy})_2]_n \cdot 2n$DMF (**9**·2DMF)

$[Fe_2MnO(OAc)_6(H_2O)_3]$ (0.1 g, 0.169 mmol) was dissolved in 3 mL of DMF, followed by the addition of 15 mL of MeCN, then 0.1 mL of acetic acid was added, and then bipy (0.250 g, 0.423 mmol, a 25% excess) was dissolved in this solution. After one day black crystals formed, which were collected by filtration, washed with MeCN (2 portions by 3 mL) and dried on air. Yield 0.04 g (25%). Anal, calc. for $C_{38}H_{48}N_6O_{15}Fe_2Mn$/found, %: C 45.9/45.6, H 4.86/4.50, N 8.44/8.50.

3.2.7. Synthesis of $[MnFe_2O(OAc)_6(bpe)_2]_n \cdot 2n$DMF (10·2DMF)

$[Fe_2MnO(OAc)_6(H_2O)_3]$ (0.1 g, 0.169 mmol) was dissolved in 3 mL of DMF, followed by the addition of 15 mL of MeCN. Next 0.1 mL of acetic acid was added, and then bpe (0.185 g, 0.014 mmol, a 3-fold excess) was dissolved in this solution. After one day black crystals formed, which were collected by filtration, washed with MeCN (2 portions by 3 mL) and dried on air. Yield 0.07 g (40%). Anal, calc. for $C_{42}H_{52}N_6O_{15}Fe_2Mn$ / found, %: C 48.2/48.1, H 5.00/5.15, N 8.02/7.98.

3.2.8. Synthesis of $[MnFe_2O(OAc)_6(bpe)(DMF)]_n \cdot 3.5n$DMF (11·3.5DMF)

$[Fe_2MnO(OAc)_6(H_2O)_3]$ (0.1 g, 0.169 mmol) was dissolved in 3 mL of DMF, followed by the addition of 15 mL of MeCN. Next 0.1 mL of acetic acid was added, and then bpe (0.038 g, 0.211 mmol, a 25% excess) was dissolved in this solution. After one day black crystals formed, which were collected by filtration, washed with MeCN (two portions of 3 mL) and dried on air. Yield 0.02 g (10%). Anal, calc. for $C_{34.5}H_{52.5}N_{5.5}O_{16.5}Fe_2Mn$/found, %: C 42.5/42.1, H 5.43/5.35, N 7.90/7.95.

3.3. X-ray Structure Determination

For X-ray structure determination single crystals of the compounds **1**–**8** were isolated from the mother liquors and mounted on a Bruker APEX II diffractometer equipped with a CCD camera and a graphite monochromated MoK_α radiation source (λ = 0.71073 Å) at the N. S. Kurnakov Institute of General and Inorganic Chemistry (Moscow, Russia). X-ray structure determination for compounds **9**–**11** was performed using a a Kappa-Nonius four circle diffractometer equipped with a CCD camera and a graphite monochromated MoK_α radiation source (λ = 0.71073 Å), located at the Centre de Diffractométrie (CDIFX), Université de Rennes 1 (Rennes, France).

Effective absorption correction was performed using SCALEPACK. Structures of the complexes were solved by the direct method using SHELXS-97 [85] or Sir-97 [86] software, and refined with a full matrix least squares method on F^2 using SHELXL-97, SHELX-2014 or SHELX-2018 program [87]. H atoms were treated by a riding model. Solvent molecules, which could not be localized, were removed by SQUEEZE procedure for compounds **9**–**11** [88]. The structure of **6** was solved taking into account crystal twinning (Flack parameter is 0.42(4)). Crystallographic data and structure refinement parameters for **1**–**11** are presented in Tables 2–4. Supplementary crystallographic data for the compounds synthesized are given in CCDC numbers 2055493-2055503 for **1**–**11**, respectively. These data can be obtained free of charge from The Cambridge Crystallographic Data Centre via www.ccdc.cam.ac.uk/data_request/cif.

Table 2. Crystallographic data and structure refinement parameters for **1**–**4**.

	1	**2**	**3**·**MeCN**	**4**·**0.5MeCN**
Empirical formula	$C_{40}H_{52}Mn_2N_4O_8$	$C_{44}H_{52}Mn_2N_4O_8$	$C_{52}H_{73}Mn_4N_5O_{14}$	$C_{55}H_{71.5}Mn_4N_{4.5}O_{14}$
Formula weight (g·mol^{-1})	826.73	874.77	1211.91	1239.42
T/K	150(2)	296(2)	296(2)	296(2)
Crystal system	Monoclinic	Monoclinic	Monoclinic	Monoclinic
Space group	$P2_1/c$	$C2/c$	$P2_1/c$	$P2_1/n$
a (Å)	11.676(6)	19.821(16)	12.7090(14)	12.752(4)
b (Å)	18.715(10)	17.592(14)	18.925(2)	16.007(5)
c (Å)	9.859(5)	13.907(11)	14.094(2)	16.088(5)
α (°)	90	90	90	90
β (°)	107.922(8)	115.565(12)	104.947(2)	92.761(5)
γ (°)	90	90	90	90
V (Å^3)	2049.9(19)	4374(6)	3275.2(6)	3280.0(16)
Z	2	4	2	2
D_{calc} (g·cm^{-3})	1.339	1.328	1.229	1.255
μ (mm^{-1})	0.67	0.632	0.811	0.811
F(000)	868	1832	1264	1290
θ range for data collection (°)	1.83 to 26.37	1.62 to 26.70	1.66 to 28.13	1.80 to 26.44
Reflections collected	14,993	16,361	20,634	29,369
Reflections unique	4194	4605	7934	6685
R_{int}	0.162	0.069	0.044	0.070
Parameters	257	262	409	439
GOF	0.900	1.037	1.010	1.004
R_1 [a] [$I_o > 2\sigma I$)]	0.052	0.059	0.053	0.059
wR_2 [b] [$I_o > 2\sigma I$)]	0.099	0.155	0.128	0.172

[a] $R_1 = \Sigma||Fo| - |Fc||/\Sigma|Fo|$. [b] $wR_2 = \{\Sigma[w(Fo^2 - Fc^2)^2]/\Sigma[w(Fo^2)^2]\}^{1/2}$.

Table 3. Crystallographic data and structure refinement parameters for **5**–**8**.

	5	**6**	**7**·**2MeCN**	**8**
Empirical formula	$C_{66}H_{108}Mn_6N_8O_{22}$	$C_{58}H_{98}Mn_6N_4O_{22}$	$C_{47}H_{78}Mn_4N_6O_{15}$	$C_{72}H_{128}Fe_2Mn_4N_6O_{26}$
Formula weight (g·mol^{-1})	1695.24	1533.04	1186.91	1825.26
T/K	173(2)	296(2)	173(2)	150(2)
Crystal system	Monoclinic	Monoclinic	Triclinic	Monoclinic
Space group	$P2_1/n$	Pn	$P^{-}1$	$C2/c$
a (Å)	13.7821(10)	14.404(3)	13.4652(18)	13.4462(15)
b (Å)	21.676(2)	16.331(3)	13.7324(18)	29.008(3)
c (Å)	13.8218(10)	16.330(3)	18.150(2)	23.868(3)
α (°)	90	90	111.943(2)	90
β (°)	98.7840(10)	103.009(3)	90.612(2)	91.930(2)
γ (°)	90	90	103.879(2)	90
V (Å^3)	4080.8(5)	3742.6(14)	3003.2(7)	9304.3(18)
Z	2	2	2	4
D_{calc} (g·cm^{-3})	1.380	1.360	1.313	1.303
μ (mm^{-1})	0.971	1.050	0.884	0.900
F(000)	1772	1600	1244	3848
θ range for data collection (°)	1.76 to 26.60	1.25 to 28.27	1.22 to 26.90	1.40 to 28.28
Reflections collected	30,266	21,851	28,737	39,848
Reflections unique	8537	14,323	12,922	11,443
R_{int}	0.052	0.054	0.047	0.097
Parameters	460	813	716	542
GOF	0.990	0.969	1.052	1.025
R_1 [a] [$I_o > 2\sigma I$)]	0.046	0.082	0.056	0.058
wR_2 [b] [$I_o > 2\sigma I$)]	0.131	0.199	0.148	0.126

[a] $R_1 = \Sigma||Fo| - |Fc||/\Sigma|Fo|$. [b] $wR_2 = \{\Sigma[w(Fo^2 - Fc^2)^2]/\Sigma[w(Fo^2)^2]\}^{1/2}$.

Table 4. Crystallographic data and structure refinement parameters for **9**–**11**.

	9	**10**	**11**
Empirical formula	$C_{64}H_{68}Fe_4Mn_2N_8O_{26}$	$C_{36}H_{37.5}Fe_2MnN_4O_{13}$	$C_{27}H_{35}Fe_2MnN_3O_{14}$
Formula weight ($g \cdot mol^{-1}$)	1698.54	900.84	792.22
T/K	293(2)	293(2)	293(2)
Crystal system	Monoclinic	Triclinic	Orthorhombic
Space group	$I2/a$	$P^{-}1$	$P2_12_12_1$
a (Å)	20.0570(6)	12.889(5)	8.0410(1)
b (Å)	25.1754(7)	14.469(5)	19.572(1)
c (Å)	34.7618(11)	16.096(5)	30.223(1)
α (°)	90	88.749(5)	90
β (°)	68.184(2)	66.401(5)	90
γ (°)	90	87.004(5)	90
V ($Å^3$)	17,374.0(9)	2747.0(17)	4756.5(7)
Z	8	2	4
D_{calc} ($g \cdot cm^{-3}$)	1.391	1.089	1.106
μ (mm^{-1})	1.012	0.796	0.912
F(000)	7472	925	1628
θ range for data collection (°)	5.09 to 25.56	2.76 to 26.37	1.24 to 25.68
Reflections collected	43,517	14,357	14,696
Reflections unique	15,023	9780	7253
R_{int}	0.147	0.041	0.100
Parameters	941	505	425
GOF	1.084	1.001	0.989
R_1 [a] [$I_o > 2\sigma I$)]	0.107	0.101	0.095
wR_2 [b] [$I_o > 2\sigma I$)]	0.199	0.291	0.248

[a] $R_1 = \Sigma||Fo| - |Fc||/\Sigma|Fo|$. [b] $wR_2 = \{\Sigma[w(Fo^2 - Fc^2)^2]/\Sigma[w(Fo^2)^2]\}^{1/2}$.

3.4. DFT Calculations

The signs and the magnitudes of exchange coupling parameters J were independently estimated by DFT calculations similar to the previously reported by us in details [89], brief description of the methodology is provided in this section.

The calculations were performed via ORCA software [90]. TPSSh [91–93] exchange-correlation potential was employed for the calculation together with LANLTZ basis sets [94] for 3d ions and def2-SVP [95] basis set for the rest of the elements.

The atomic coordinates were taken from the crystallographic data. For calculation of each J value, all Mn^{2+} ions in Mn_4 core except the two ions taking part in the coupling were "substituted" by diamagnetic Zn^{2+} ions in order to simplify the system of spin states of the species. Broken symmetry DFT approach was applied for the calculation of J: first, a single-point calculation was performed for the high-spin state of the Mn_2Zn_2 species, then the broken symmetry state was constructed by artificial flipping the spin projections of the unpaired electrons localized on one of the Mn^{2+} ions, and a single-point calculation was performed again. J value was obtained using the energies E_{HS} and E_{BS} resulted from the two converged single-point calculations as $J = -(E_{HS} - E_{BS})/(<S^2>_{HS} - <S^2>_{BS})$ [96] ($<S^2>_{HS}$ and $<S^2>_{BS}$—the total spin operator expectation values derived from the calculations).

4. Conclusions

In this study a variety of transformations of Mn-containing complexes in reactions with N-donor heterocycles was shown. In was found that homometallic Mn pivalates underwent metamorphosis while heterometallic acetates with a Fe_2MnO core preserved their structure, giving rise to coordination polymers. Different behavior of Mn^{II} or Ni^{II} and Co^{II} pivalates in reactions with $FeCl_3$ was also revealed: while the first complex produced a hexanuclear $[Mn^{II}_4Fe^{III}_2O_2(Piv)_{10}(MeCN)_2(HPiv)_2]$ compound, the latter (Ni^{II} and Co^{II}) pivalates under similar conditions gave trinuclear pivalates with a Fe_2MnO core.

Several new coordination polymers with bridging pyrimidine (i.e., $[Mn_6O_2(Piv)_{10}(pym)_2]_n$), 4,4-bipyridine (i.e., $[MnFe_2O(OAc)_6(4,4'\text{-bipy})_2]_n$) or 1,2-*bis*-trans-(4-pyridyl)ethylene (i.e.,

$[MnFe_2O(OAc)_6(bpe)_2]_n$ and $[MnFe_2O(OAc)_6(bpe)(DMF)]_n$) were prepared. Unexpectedly, the composition of the coordination polymers based on $MnFe_2O(OAc)_6$ was probably governed by a fine balance between formation and crystallization kinetics and solubility of certain species, in contrast to the ratio of potential vacations in the coordination spheres of metal ions and the number of donor atoms). The crystal lattice of $[MnFe_2O(OAc)_6(bpe)(DMF)]_n$ collapsed upon desolvatation, and the resulting compound was not porous in respect to N_2, however the porosity was restored upon interaction with methanol and ethanol. Notably, the hexanuclear unit $\{Mn^{II}_4Fe^{III}_2O_2(O_2CR)_{10}\}$ can be considered a promising new building block for the creation of coordination polymers.

Magnetic properties of the compounds were in line with those expected for Mn carboxylates. The temperature dependence of the magnetic susceptibility of $[Mn_4(\mu_3\text{-}OH)(Piv)_7(\mu\text{-}pz)_2]_n$ could be fitted with five exchange coupling parameters, and their reliability was independently checked by DFT calculations.

Supplementary Materials: The following are available online. Figure S1: PXRD data for **6**; Figure S2: Visualization of solvent-accessible voids for **9**.

Author Contributions: Conceptualization, L.O. and I.L.E.; Formal analysis, R.A.P., I.S.E., A.S.L., V.V.M., S.V.K. and M.A.K.; Investigation, R.A.P., I.S.E., O.C., S.G., K.S.G., A.S.L., N.N.E., V.V.M., A.S.B., S.V.K. and M.A.K.; Methodology, R.A.P., S.V.K. and M.A.K.; Writing—original draft, S.V.K.; Writing—review & editing, S.G., A.S.L., S.V.K. and M.A.K. All authors have read and agreed to the published version of the manuscript.

Funding: S.V.K. thanks to the National Academy of Sciences of Ukraine and University of Rennes for support. I.S.E., N.N.E., V.V.M., M.A.K. and I.L.E. thank IGIC RAS state assignment for support.

Institutional Review Board Statement: Not applicable.

Informed Consent Statement: Not applicable.

Data Availability Statement: The data presented in this study are available on request from the corresponding author.

Acknowledgments: Single crystal X-ray analysis (**1**–**8**), IR-spectroscopy, elemental analysis, magnetic (**1**, **2**, **7**) and EPR (**1**, **2**) measurements were performed using shared experimental facilities supported by IGIC RAS state assignment.

Conflicts of Interest: The authors declare no conflict of interest.

Sample Availability: Not available.

References

1. Glaser, F.; Wenger, O.S. Recent Progress in the Development of Transition-Metal Based Photoredox Catalysts. *Coord. Chem. Rev.* **2020**, *405*, 213129. [CrossRef]
2. Hazari, N.; Melvin, P.R.; Beromi, M.M. Well-Defined Nickel and Palladium Precatalysts for Cross-Coupling. *Nat. Rev. Chem.* **2017**, *1*, 0025. [CrossRef] [PubMed]
3. Cooper, B.G.; Napoline, J.W.; Thomas, C.M. Catalytic Applications of Early/Late Heterobimetallic Complexes. *Cat. Rev.* **2012**, *54*, 1–40. [CrossRef]
4. Bilyachenko, A.N.; Dronova, M.S.; Yalymov, A.I.; Lamaty, F.; Bantreil, X.; Martinez, J.; Bizet, C.; Shul'pina, L.S.; Korlyukov, A.A.; Arkhipov, D.E.; et al. Cage-like Copper(II) Silsesquioxanes: Transmetalation Reactions and Structural, Quantum Chemical, and Catalytic Studies. *Chem. Eur. J.* **2015**, *21*, 8758–8770. [CrossRef] [PubMed]
5. Kirillov, A.M.; Kirillova, M.V.; Pombeiro, A.J.L. Homogeneous Multicopper Catalysts for Oxidation and Hydrocarboxylation of Alkanes. *Adv. Inorg. Chem.* **2013**, *65*, 1–31. [CrossRef]
6. Masoomi, M.Y.; Morsali, A. Applications of Metal–Organic Coordination Polymers as Precursors for Preparation of Nano-Materials. *Coord. Chem. Rev.* **2012**, *256*, 2921–2943. [CrossRef]
7. de la Rosa, L.A.G.; Méndez-Rojas, M.A. Direct Synthesis of Nanomaterials: Building Bridges between Metal Complexes and Nanomaterials. In *Direct Synthesis of Metal Complexes*; Elsevier: Amsterdam, The Neatherlands, 2018; pp. 317–337. ISBN 978-0-12-811061-4.
8. Zauzolkova, N.; Dobrokhotova, Z.; Lermontov, A.; Zorina, E.; Emelina, A.; Bukov, M.; Chernyshev, V.; Sidorov, A.; Kiskin, M.; Bogomyakov, A.; et al. Step-by-Step Thermal Transformations of a New Porous Coordination Polymer $[(H_2O)_5CuBa(Me_2mal)_2]_n$ (Me_2mal^{2-}=dimethylmalonate): Thermal Degradation to Barium Cuprate. *J. Solid State Chem.* **2013**, *197*, 379–391. [CrossRef]

9. Maniaki, D.; Pilichos, E.; Perlepes, S.P. Coordination Clusters of 3d-Metals That Behave as Single-Molecule Magnets (SMMs): Synthetic Routes and Strategies. *Front. Chem.* **2018**, *6*, 461. [CrossRef]
10. Coronado, E. Molecular Magnetism: From Chemical Design to Spin Control in Molecules, Materials and Devices. *Nat. Rev. Mater.* **2020**, *5*, 87–104. [CrossRef]
11. Gaita-Ariño, A.; Luis, F.; Hill, S.; Coronado, E. Molecular Spins for Quantum Computation. *Nat. Chem.* **2019**, *11*, 301–309. [CrossRef]
12. Levitsky, M.M.; Bilyachenko, A.N.; Shubina, E.S.; Long, J.; Guari, Y.; Larionova, J. Magnetic cage-like metallasilsesquioxanes. *Coord. Chem. Rev.* **2019**, *398*, 213015. [CrossRef]
13. Ferrando-Soria, J.; Vallejo, J.; Castellano, M.; Martínez-Lillo, J.; Pardo, E.; Cano, J.; Castro, I.; Lloret, F.; Ruiz-García, R.; Julve, M. Molecular magnetism, *quo vadis?* A historical perspective from a coordination chemist viewpoint. *Coord. Chem. Rev.* **2017**, *339*, 17–103. [CrossRef]
14. Nandasiri, M.I.; Jambovane, S.R.; McGrail, B.P.; Schaef, H.T.; Nune, S.K. Adsorption, Separation, and Catalytic Properties of Densified Metal-Organic Frameworks. *Coord. Chem. Rev.* **2016**, *311*, 38–52. [CrossRef]
15. Jeon, I.-R.; Clérac, R. Controlled Association of Single-Molecule Magnets (SMMs) into Coordination 15.Networks: Towards a New Generation of Magnetic Materials. *Dalton Trans.* **2012**, *41*, 9569. [CrossRef]
16. Polunin, R.A.; Kolotilov, S.V.; Kiskin, M.A.; Cador, O.; Mikhalyova, E.A.; Lytvynenko, A.S.; Golhen, S.; Ouahab, L.; Ovcharenko, V.I.; Eremenko, I.L.; et al. Topology Control of Porous Coordination Polymers by Building Block Symmetry. *Eur. J. Inorg. Chem.* **2010**, *2010*, 5055–5057. [CrossRef]
17. Kolotilov, S.V.; Cador, O.; Gavrilenko, K.S.; Golhen, S.; Ouahab, L.; Pavlishchuk, V.V. Assembly of Dinuclear Cu^{II} Rigid Blocks by Bridging Azido or Poly(Thiocyanato)Chromates: Synthesis, Structures and Magnetic Properties of Coordination Polymers and Polynuclear Complexes. *Eur. J. Inorg. Chem.* **2010**, *2010*, 1255–1266. [CrossRef]
18. Lytvynenko, A.S.; Kolotilov, S.V.; Kiskin, M.A.; Cador, O.; Golhen, S.; Aleksandrov, G.G.; Mishura, A.M.; Titov, V.E.; Ouahab, L.; Eremenko, I.L.; et al. Redox-Active Porous Coordination Polymers Prepared by Trinuclear Heterometallic Pivalate Linking with the Redox-Active Nickel(II) Complex: Synthesis, Structure, Magnetic and Redox Properties, and Electrocatalytic Activity in Organic Compound Dehalogenation in Heterogeneous Medium. *Inorg. Chem.* **2014**, *53*, 4970–4979. [CrossRef] [PubMed]
19. Polunin, R.A.; Kiskin, M.A.; Cador, O.; Kolotilov, S.V. Coordination Polymers Based on Trinuclear Heterometallic Pivalates and Polypyridines: Synthesis, Structure, Sorption and Magnetic Properties. *Inorg. Chim. Acta* **2012**, *380*, 201–210. [CrossRef]
20. Botezat, O.; van Leusen, J.; Kravtsov, V.C.; Filippova, I.G.; Hauser, J.; Speldrich, M.; Hermann, R.P.; Krämer, K.W.; Liu, S.-X.; Decurtins, S.; et al. Interpenetrated (8,3)-c and (10,3)-b Metal–Organic Frameworks Based on $\{Fe^{III}{}_3\}$ and $\{Fe^{III}{}_2Co^{II}\}$ Pivalate Spin Clusters. *Cryst. Growth Des.* **2014**, *14*, 4721–4728. [CrossRef]
21. Botezat, O.; van Leusen, J.; Kögerler, P.; Baca, S.G. Tuning the Condensation Degree of $\{Fe^{III}{}_n\}$ Oxo Clusters via Ligand Metathesis, Temperature, and Solvents. *Inorg. Chem.* **2018**, *57*, 7904–7913. [CrossRef]
22. Botezat, O.; van Leusen, J.; Kravtsov, V.C.; Kögerler, P.; Baca, S.G. Ultralarge 3d/4f Coordination Wheels: From Carboxylate/Amino Alcohol-Supported $\{Fe_4Ln_2\}$ to $\{Fe_{18}Ln_6\}$ Rings. *Inorg. Chem.* **2017**, *56*, 1814–1822. [CrossRef]
23. Taguchi, T.; Daniels, M.R.; Abboud, K.A.; Christou, G. Mn_4, Mn_6, and Mn_{11} Clusters from the Use of Bulky Diphenyl(pyridine-2-yl)methanol. *Inorg. Chem.* **2009**, *48*, 9325–9335. [CrossRef] [PubMed]
24. Mondal, K.C.; Song, Y.; Mukherjee, P.S. Self-Assembly of a Mn_9 Nanoscopic Mixed-Valent Cluster: Synthesis, Crystal Structure, and Magnetic Behavior. *Inorg. Chem.* **2007**, *46*, 9736–9742. [CrossRef]
25. Wemple, M.W.; Tsai, H.-L.; Wang, S.; Claude, J.P.; Streib, W.E.; Huffman, J.C.; Hendrickson, D.N.; Christou, G. Tetranuclear and Octanuclear Manganese Carboxylate Clusters: Preparation and Reactivity of $(NBu^n{}_4)[Mn_4O_2(O_2CPh)_9(H_2O)]$ and Synthesis of $(Nbu^n{}_4)_2[Mn_8O_4(O_2CPh)_{12}(Et_2Mal)_2(H_2O)_2]$ with a "Linked-Butterfly" Structure. *Inorg. Chem.* **1996**, *35*, 6437–6449. [CrossRef]
26. Boskovic, C.; Wernsdorfer, W.; Folting, K.; Huffman, J.C.; Hendrickson, D.N.; Christou, G. Single-Molecule Magnets: Novel Mn_8 and Mn_9 Carboxylate Clusters Containing an Unusual Pentadentate Ligand Derived from Pyridine-2,6-Dimethanol. *Inorg. Chem.* **2002**, *41*, 5107–5118. [CrossRef]
27. Polunin, R.A.; Kolotilov, S.V.; Kiskin, M.A.; Gavrilenko, K.S.; Ouahab, L.; Eremenko, I.L.; Novotortsev, V.M.; Pavlishchuk, V.V. Structures and Sorption Properties of the Coordination Polymers Built up of 3d Metal Carboxylate Polynuclear Complexes. *Russ. Chem. Bull.* **2010**, *59*, 1217–1224. [CrossRef]
28. Köberl, M.; Cokoja, M.; Herrmann, W.A.; Kühn, F.E. From Molecules to Materials: Molecular Paddle-Wheel Synthons of Macromolecules, Cage Compounds and Metal–Organic Frameworks. *Dalton Trans.* **2011**, *40*, 6834. [CrossRef] [PubMed]
29. Duncan, J.F.; Kanekar, C.R.; Mok, K.F. Some Trinuclear Iron(III) Carboxylate Complexes. *J. Chem. Soc. Inorg. Phys. Theor.* **1969**, 480–482. [CrossRef]
30. Blake, A.B.; Yavari, A.; Hatfield, W.E.; Sethulekshmi, C.N. Magnetic and Spectroscopic Properties of Some Heterotrinuclear Basic Acetates of Chromium(III), Iron(III), and Divalent Metal Ions. *J. Chem. Soc. Dalton Trans.* **1985**, 2509–2520. [CrossRef]
31. Gavrilenko, K.S.; Vértes, A.; Vanko, G.; Kiss, L.F.; Addison, A.W.; Weyhermüller, T.; Pavlishchuk, V.V. Synthesis, Magnetochemistry, and Spectroscopy of Heterometallic Trinuclear Basic Trifluoroacetates $[Fe_2M(\mu_3\text{-}O)(CF_3COO)_6(H_2O)_3]\cdot H_2O$ (M = Mn, Co, Ni). *Eur. J. Inorg. Chem.* **2002**, *2002*, 3347–3355. [CrossRef]
32. Lytvynenko, A.S.; Kolotilov, S.V.; Cador, O.; Gavrilenko, K.S.; Golhen, S.; Ouahab, L.; Pavlishchuk, V.V. Porous 2D Coordination Polymeric Formate Built up by Mn(II) Linking of Fe_3O Units: Influence of Guest Molecules on Magnetic Properties. *Dalton Trans.* **2009**, 3503–3509. [CrossRef]

33. Kiskin, M.; Zorina-Tikhonova, E.; Kolotilov, S.; Goloveshkin, A.; Romanenko, G.; Efimov, N.; Eremenko, I. Synthesis, Structure, and Magnetic Properties of a Family of Complexes Containing a $Co^{II}_2Dy^{III}$ Pivalate Core and a Pentanuclear $Co^{II}_4Dy^{III}$ Derivative. *Eur. J. Inorg. Chem.* **2018**, *2018*, 1356–1366. [CrossRef]
34. Burkovskaya, N.P.; Orlova, E.V.; Kiskin, M.A.; Efimov, N.N.; Bogomyakov, A.S.; Fedin, M.V.; Kolotilov, S.V.; Minin, V.V.; Aleksandrov, G.G.; Sidorov, A.A.; et al. Synthesis, Structure, and Magnetic Properties of Heterometallic Trinuclear Complexes $\{M^{II}—Ln^{III}—M^{II}\}$ (M^{II} = Ni, Cu; Ln^{III} = La, Pr, Sm, Eu, Gd). *Russ. Chem. Bull.* **2011**, *60*, 2490–2503. [CrossRef]
35. Lutsenko, I.A.; Kiskin, M.A.; Nikolaevskii, S.A.; Starikova, A.A.; Efimov, N.N.; Khoroshilov, A.V.; Bogomyakov, A.S.; Ananyev, I.V.; Voronina, J.K.; Goloveshkin, A.S.; et al. Ferromagnetically Coupled Molecular Complexes with a $Co^{II}_2Gd^{III}$ Pivalate Core: Synthesis, Structure, Magnetic Properties and Thermal Stability. *ChemistrySelect* **2019**, *4*, 14261–14270. [CrossRef]
36. Reynolds, R.A.; Dunham, W.R.; Coucouvanis, D. Kinetic Lability, Structural Diversity, and Oxidation Reactions of New Oligomeric, Anionic Carboxylate−Pyridine Complexes. *Inorg. Chem.* **1998**, *37*, 1232–1241. [CrossRef] [PubMed]
37. Yamaguchi, K.S.; Sawyer, D.T. The Redox Chemistry of Manganese(III) and –(IV) Complexes. *Isr. J. Chem.* **1985**, *25*, 164–176. [CrossRef]
38. Pedersen, K.S.; Bendix, J.; Clérac, R. Single-Molecule Magnet Engineering: Building-Block Approaches. *Chem. Commun.* **2014**, *50*, 4396–4415. [CrossRef]
39. Dincă, M.; Long, J.R. High-Enthalpy Hydrogen Adsorption in Cation-Exchanged Variants of the Microporous Metal−Organic Framework $Mn_3[(Mn_4Cl)_3(BTT)_8(CH_3OH)_{10}]_2$. *J. Am. Chem. Soc.* **2007**, *129*, 11172–11176. [CrossRef]
40. Kar, P.; Haldar, R.; Gómez-García, C.J.; Ghosh, A. Antiferromagnetic Porous Metal–Organic Framework Containing Mixed-Valence $[Mn^{II}_4Mn^{III}_2(\mu_4\text{-}O)_2]^{10+}$ Units with Catecholase Activity and Selective Gas Adsorption. *Inorg. Chem.* **2012**, *51*, 4265–4273. [CrossRef]
41. Li, C.-X.; Zeng, D.-F.; Chen, Y.-P.; Zhang, H.-H.; Sun, Y.-Q.; Chai, X.-C.; Lei, R.; Sun, R.-Q.; Huaxue, J. Syntheses and Crystal Structures of Two New Compounds: $[Zn(2,2'\text{-bipy})(L)Cl]_2$ and $[Zn(phen)(L2)]_2$ (HL—3-Methylbenzoic Acid). *Chin. J. Struct. Chem.* **2009**, *28*, 1381–1386.
42. Perlepes, S.P.; Libby, E.; Streib, W.E.; Folting, K.; Christou, G. The Reactions of $Cu_2(O_2CMe)_4(H_2O)_2$ with 2,2′-Bipyridine (Bpy): Influence of the Cu: Bpy Ratio, and the Structure of a Linear Polymer Comprising Two Alternating Types of Cu_2 Units. *Polyhedron* **1992**, *11*, 923–936. [CrossRef]
43. Talismanova, M.O.; Sidorov, A.A.; Novotortsev, V.M.; Aleksandrov, G.G.; Nefedov, S.E.; Eremenko, I.L.; Moiseev, I.I. Unusual Transformation of the Urea Molecule Giving Rise to the NCO^- Anion as a Bridging Ligand between Two Co^{II} Atoms. *Russ. Chem. Bull.* **2001**, *50*, 2251–2253. [CrossRef]
44. Zhang, Q.-Z.; Lu, C.-Z. Di-μ-Acetato-Bis[Bis(4-Aminobenzoato)(2,2′-Bipyridyl)Manganese(II)]. *Acta Crystallogr. C* **2005**, *61*, m78–m80. [CrossRef]
45. Banerjee, S.; Rajakannu, P.; Butcher, R.J.; Murugavel, R. Auxiliary Ligand-Aided Tuning of Aggregation of Transition Metal Benzoates: Isolation of Four Different Types of Coordination Polymers. *CrystEngComm* **2014**, *16*, 8429–8441. [CrossRef]
46. Goldberg, A.E.; Kiskin, M.A.; Kozyukhin, S.A.; Sidorov, A.A.; Eremenko, I.L. Binuclear Zinc Naphthoate Complex with 1,10-Phenanthroline: Synthesis, Structure, and Photoluminescence Properties. *Russ. Chem. Bull.* **2011**, *60*, 1012–1015. [CrossRef]
47. Dey, D.; Roy, S.; Dutta Purkayastha, R.N.; Pallepogu, R.; McArdle, P. Zinc Carboxylates Containing Diimine: Synthesis, Characterization, Crystal Structure, and Luminescence. *J. Mol. Struct.* **2013**, *1053*, 127–133. [CrossRef]
48. Li, X.-M.; Wang, Q.-W.; Liu, B.; Huaxue, J. Synthesis and Crystal Structure of a Zinc(II) Complex with 2-(4′-Chlorine-benzoyl)-benzoic Acid and 1,10-Phenanthroline. *Chin. J. Struct. Chem.* **2011**, *30*, 1646–1649.
49. Baca, S.G.; Malaestean, I.L.; Keene, T.D.; Adams, H.; Ward, M.D.; Hauser, J.; Neels, A.; Decurtins, S. One-Dimensional Manganese Coordination Polymers Composed of Polynuclear Cluster Blocks and Polypyridyl Linkers: Structures and Properties. *Inorg. Chem.* **2008**, *47*, 11108–11119. [CrossRef]
50. Evstifeev, I.S.; Kiskin, M.A.; Mironov, V.S.; Bogomyakov, A.S.; Sidorov, A.A.; Novotortsev, V.M.; Eremenko, I.L. 1D Nickel(II) Coordination Polymer with Pyrimidine and Pivalate Bridges: Synthesis, Structure and Magnetic Properties. *Inorg. Chem. Commun.* **2010**, *13*, 498–501. [CrossRef]
51. Kiskin, M.A.; Fomina, I.G.; Aleksandrov, G.G.; Sidorov, A.A.; Novotortsev, V.M.; Rakitin, Y.V.; Dobrokhotova, Z.V.; Ikorskii, V.N.; Shvedenkov, Y.G.; Eremenko, I.L.; et al. New Antiferromagnetic Mn(II) Pivalate Polymer: Synthesis and Reactivity. *Inorg. Chem. Commun.* **2005**, *8*, 89–93. [CrossRef]
52. Nakata, K.; Miyasaka, H.; Sugimoto, K.; Ishii, T.; Sugiura, K.; Yamashita, M. Construction of a One-Dimensional Chain Composed of Mn_6 Clusters and 4,4′-Bipyridine Linkers: The First Step for Creation of "Nano-Dots-Wires". *Chem. Lett.* **2002**, *31*, 658–659. [CrossRef]
53. Kar, P.; Ida, Y.; Ishida, T.; Ghosh, A. Formation of Two Drastically Different MOFs Based on Mn(II)–Benzoate and Pyrazine with a Change in Seasonal Temperature: Structural Analysis and Magnetic Study. *CrystEngComm* **2012**, *15*, 400–410. [CrossRef]
54. Kar, P.; Ida, Y.; Kanetomo, T.; Drew, M.G.B.; Ishida, T.; Ghosh, A. Synthesis of Mixed-Valence Hexanuclear Mn(II/III) Clusters from Its Mn(II) Precursor: Variations of Catecholase-like Activity and Magnetic Coupling. *Dalton Trans.* **2015**, *44*, 9795–9804. [CrossRef]
55. Malaestean, I.L.; Kravtsov, V.C.; Speldrich, M.; Dulcevscaia, G.; Simonov, Y.A.; Lipkowski, J.; Ellern, A.; Baca, S.G.; Kögerler, P. One-Dimensional Coordination Polymers from Hexanuclear Manganese Carboxylate Clusters Featuring a $\{Mn^{II}_4Mn^{III}_2(\mu_4\text{-}O)_2\}$ Core and Spacer Linkers. *Inorg. Chem.* **2010**, *49*, 7764–7772. [CrossRef] [PubMed]

56. Sañudo, E.C.; Cauchy, T.; Ruiz, E.; Laye, R.H.; Roubeau, O.; Teat, S.J.; Aromí, G. Molecules Composed of Two Weakly Magnetically Coupled [Mn^{III}_4] Clusters. *Inorg. Chem.* **2007**, *46*, 9045–9047. [CrossRef] [PubMed]
57. Abdulwahab, K.O.; Malik, M.A.; O'Brien, P.; Timco, G.A.; Tuna, F.; Muryn, C.A.; Winpenny, R.E.P.; Pattrick, R.A.D.; Coker, V.S.; Arenholz, E. A One-Pot Synthesis of Monodispersed Iron Cobalt Oxide and Iron Manganese Oxide Nanoparticles from Bimetallic Pivalate Clusters. *Chem. Mater.* **2014**, *26*, 999–1013. [CrossRef]
58. Dulcevscaia, G.M.; Filippova, I.G.; Speldrich, M.; van Leusen, J.; Kravtsov, V.C.; Baca, S.G.; Kögerler, P.; Liu, S.-X.; Decurtins, S. Cluster-Based Networks: 1D and 2D Coordination Polymers Based on {$MnFe_2(\mu_3$-O)}-Type Clusters. *Inorg. Chem.* **2012**, *51*, 5110–5117. [CrossRef]
59. Novitchi, G.; Helm, L.; Anson, C.; Powell, A.K.; Merbach, A.E. NMR Study of Ligand Exchange and Electron Self-Exchange between Oxo-Centered Trinuclear Clusters [$Fe_3(\mu_3$-O)(μ-$O_2CR)_6$(4-R′py)$_3$]$^{+/0}$. *Inorg. Chem.* **2011**, *50*, 10402–10416. [CrossRef]
60. Liu, J.-Q.; Wu, T. Crystal Structure of (2,2′-Bipyridine)-(Adamantane-1,3-Dicarboxylato)- Manganese(II) Hydrate, Mn($C_{10}H_8N_2$)($C_{12}H_{14}O_4$)·H_2O. *Z. Für Krist.—New Cryst. Struct.* **2010**, *225*, 483–485. [CrossRef]
61. Ma, Y.-S.; Tang, X.-Y.; Xue, F.-F.; Chen, B.; Dai, Y.-L.; Yuan, R.-X.; Roy, S. Structural Diversity and Magnetic Properties of the Manganese(II)/Carbazol-9-ylacetate/N,N′-Donor Reaction System. *Eur. J. Inorg. Chem.* **2012**, *2012*, 1243–1249. [CrossRef]
62. Wu, D.-H.; Shi, J.; Shi, Y.-J.; Jiang, G.-Q. Tetrakis(μ-Phenoxyacetato-κ^2O:O′)Bis[(1,10-Phenanthroline-κ^2N,N′)Manganese(II)] Methanol Hemisolvate. *Acta Crystallogr. Sect. E Struct. Rep. Online* **2008**, *64*, m161. [CrossRef] [PubMed]
63. Albela, B.; El Fallah, M.S.; Ribas, J.; Folting, K.; Christou, G.; Hendrickson, D.N. Two New Mixed-Valence Manganese Complexes of Formula [Mn_4O_2(X-Benzoato)$_7$(Bpy)$_2$] (X = 2-Cl, 2-Br) and the Crystal Structure of the 2-Cl Complex: Ground-State Spin Variability in the [Mn_4O_2]$^{7+}$ Complexes. *Inorg. Chem.* **2001**, *40*, 1037–1044. [CrossRef]
64. Pistilli, J.; Beer, R.H. A Tetranuclear Manganese Oxo Complex with Terminal and Bridging Trifluoroacetate Ligands: Synthesis and Structure of [$Mn_4O_2(O_2CCF_3)_8$(Bpy)$_2$]. *Inorg. Chem. Commun.* **2002**, *5*, 206–210. [CrossRef]
65. Cañada-Vilalta, C.; Huffman, J.C.; Christou, G. Preparation, Crystal Structure and Chelate Substitution Reactions of [$Mn_4O_2(O_2CPh)_6$(Dpm)$_2$] (Dpm=the Anion of Dipivaloylmethane). *Polyhedron* **2001**, *20*, 1785–1793. [CrossRef]
66. Basler, R.; Chaboussant, G.; Cañada-Vilalta, C.; Christou, G.; Mutka, H.; Janssen, S.; Altorfer, F.; Güdel, H.-U. Magnetic and Inelastic Neutron Scattering Studies of a Frustrated Tetranuclear Mn^{3+} Butterfly-Type Cluster. *Polyhedron* **2003**, *22*, 2471–2479. [CrossRef]
67. Saines, P.J.; Jain, P.; Cheetham, A.K. Evolution of the Structures and Magnetic Properties of the Manganese Dicarboxylates, $Mn_2(CO_2(CH_2)NCO_2)(OH)_2$ and $Mn_4(CO_2(CH_2)NCO_2)_3(OH)_2$. *Chem. Sci.* **2011**, *2*, 1929–1939. [CrossRef]
68. Mahata, P.; Prabu, M.; Natarajan, S. Role of Temperature and Time in the Formation of Infinite −M−O−M− Linkages and Isolated Clusters in MOFs: A Few Illustrative Examples. *Inorg. Chem.* **2008**, *47*, 8451–8463. [CrossRef] [PubMed]
69. Kiskin, M.A.; Aleksandrov, G.G.; Dobrokhotova, Z.V.; Novototrtsev, V.M.; Shvedenkov, Y.G.; Eremenko, I.L. Transformations of High Spin Mn^{II} and Fe^{II} Polymeric Pivalates in Reactions with Pivalic Acid and O-Phenylenediamines. *Russ. Chem. Bull.* **2006**, *55*, 806–820. [CrossRef]
70. Reynolds, R.A.; Yu, W.O.; Dunham, W.R.; Coucouvanis, D. Synthesis and Characterization of a New Class of μ_3-OH-Bridged Trimers That Contain Octahedrally Coordinated Divalent Metal Ions Bridged by Three Acetate Ligands and a Unique Catecholate Ligand. Solid State Molecular Structures of the [(Py)$_5M^{II}_3$(OAc)$_3$(μ_3-OH)(Cat)] Complexes (M = Mn(II), Fe(II), Co(II), Ni(II)). *Inorg. Chem.* **1996**, *35*, 2721–2722. [CrossRef]
71. Baikie, A.R.E.; Howes, A.J.; Hursthouse, M.B.; Quick, A.B.; Thornton, P. Preparation, Crystal Structure, Magnetic Properties, and Chemical Reactions of a Hexanuclear Mixed Valence Manganese Carboxylate. *J. Chem. Soc. Chem. Commun.* **1986**, 1587. [CrossRef]
72. Köhler, K.; Roesky, H.W.; Noltemeyer, M.; Schmidt, H.-G.; Freire-Erdbrügger, C.; Sheldrick, G.M. Neue Beiträge Zur Chemie Des Mangans: Synthese Und Strukturen Zweier Monomerer Mn^{II}1-Verbindungen Und Eines Hexanuklearen $Mn^{II/III}$1-Komplexes. *Chem. Ber.* **1993**, *126*, 921–926. [CrossRef]
73. Murrie, M.; Parsons, S.; Winpenny, R.E.P. Deltahedra as Underlying Structural Motifs in Polynuclear Metal Chemistry: Structure of an Undecanuclear Manganese–Potassium Cage. *J. Chem. Soc. Dalton Trans.* **1998**, *0*, 1423–1424. [CrossRef]
74. Gavrilenko, K.S.; Punin, S.V.; Cador, O.; Golhen, S.; Ouahab, L.; Pavlishchuk, V.V. Synthesis, Structure, and Magnetism of Heterometallic Carboxylate Complexes [$Mn^{III}_2M^{II}_4O_2$(PhCOO)$_{10}$(DMF)$_4$], M = Mn^{II}, Co^{II}, Ni^{II}. *Inorg. Chem.* **2005**, *44*, 5903–5910. [CrossRef] [PubMed]
75. Addison, A.W.; Rao, T.N.; Reedijk, J.; van Rijn, J.; Verschoor, G.C. Synthesis, Structure, and Spectroscopic Properties of Copper(II) Compounds Containing Nitrogen–Sulphur Donor Ligands; the Crystal and Molecular Structure of Aqua[1,7-bis(N-methylbenzimidazol-2′-yl)-2,6-dithiaheptane]copper(II) Perchlorate. *J. Chem. Soc. Dalton Trans.* **1984**, 1349–1356. [CrossRef]
76. Spek, A.L. PLATON, An Integrated Tool for the Analysis of the Results of a Single Crystal Structure Determination. *Acta Crystallogr. Sect. A* **1990**, *46*, c34. [CrossRef]
77. Férey, G.; Serre, C. Large Breathing Effects in Three-Dimensional Porous Hybrid Matter: Facts, Analyses, Rules and Consequences. *Chem. Soc. Rev.* **2009**, *38*, 1380–1399. [CrossRef]
78. Rakitin, Y.V.; Larin, G.M.; Minin, V.V. *Interpretation of EPR Spectra of Coordination Compounds*; Nauka: Moscow, Russia, 1993.
79. Belford, G.G.; Belford, R.L.; Burkhalter, J.F. Eigenfields: A Practical Direct Calculation of Resonance Fields and Intensities for Field-Swept Fixed-Frequency Spectrometers. *J. Magn. Reason.* **1969**, *11*, 251–265. [CrossRef]
80. Kahn, O. *Molecular Magnetism*; Wiley: Hoboken, NJ, USA, 1993; ISBN 978-0-471-18838-4.

81. Ma, C.; Chen, C.; Liu, Q.; Liao, D.; Li, L.; Sun, L. Structural Transformation Mediated by o-, m-, and p-Phthalates from Two to Three Dimensions for Manganese/Phthalate/4,4′-Bpy Complexes (4,4′-Bpy = 4,4′-Bipyridine). *New J. Chem.* **2003**, *27*, 890–894. [CrossRef]
82. Ma, C.; Hu, M.; Chen, C.; Liu, Q. Designed Construction of a Non-Interpenetrated 2D Bilayer Framework with Large Guest-Clathrated Channels. *Inorg. Chem. Commun.* **2005**, *8*, 219–221. [CrossRef]
83. Litvinenko, A.S.; Mikhaleva, E.A.; Kolotilov, S.V.; Pavlishchuk, V.V. Effect of Spin–Orbit Coupling on the Magnetic Susceptibility of Polynuclear Complexes of 3d Metals Containing a Co^{2+} Ion. *Theor. Exp. Chem.* **2011**, *46*, 422–428. [CrossRef]
84. Shcherbakov, I.N.; Ivanova, T.M.; Kiskin, M.A.; Kolotilov, S.V.; Novotortsev, V.M.; Eremenko, I.L.; Kogan, V.A. Computational Study of Exchange Coupling in Homo- and Heterometallic Oxo- and Carboxylato Bridged Trinuclear Complexes with Triangular $\{Fe^{III}_2M(\mu_3\text{-}O)\}$ ($M=Fe^{III}$, Ni^{II}, Co^{II}) Core. *Inorg. Chim. Acta* **2014**, *421*, 507–512. [CrossRef]
85. Sheldrick, G.M. A Short History of SHELX. *Acta Crystallogr. A* **2008**, *64*, 112–122. [CrossRef] [PubMed]
86. Altomare, A.; Burla, M.C.; Camalli, M.; Cascarano, G.L.; Giacovazzo, C.; Guagliardi, A.; Moliterni, A.G.; Polidori, G.; Spagna, R. SIR97: A New Tool for Crystal Structure Determination and Refinement. *J. Appl. Crystallogr.* **1999**, *32*, 115–119. [CrossRef]
87. Sheldrick, G.M. Crystal Structure Refinement with *SHELXL*. *Acta Crystallogr. Sect. C Struct. Chem.* **2015**, *71*, 3–8. [CrossRef] [PubMed]
88. van der Sluis, P.; Spek, A.L. BYPASS: An Effective Method for the Refinement of Crystal Structures Containing Disordered Solvent Regions. *Acta Crystallogr. Sect. A* **1990**, *46*, 194–201. [CrossRef]
89. Lutsenko, I.A.; Kiskin, M.A.; Efimov, N.N.; Ugolkova, E.A.; Maksimov, Y.V.; Imshennik, V.K.; Goloveshkin, A.S.; Khoroshilov, A.V.; Lytvynenko, A.S.; Sidorov, A.A.; et al. New Heterometallic Pivalates with Fe^{III} and Zn^{II} Ions: Synthesis, Structures, Magnetic, Thermal Properties. *Polyhedron* **2017**, *137*, 165–175. [CrossRef]
90. Neese, F. The ORCA Program System. *Wiley Interdiscip. Rev. Comput. Mol. Sci.* **2012**, *2*, 73–78. [CrossRef]
91. Staroverov, V.N.; Scuseria, G.E.; Tao, J.; Perdew, J.P. Comparative Assessment of a New Nonempirical Density Functional: Molecules and Hydrogen-Bonded Complexes. *J. Chem. Phys.* **2003**, *119*, 12129–12137. [CrossRef]
92. Staroverov, V.N.; Scuseria, G.E.; Tao, J.; Perdew, J.P. Erratum: "Comparative Assessment of a New Nonempirical Density Functional: Molecules and Hydrogen-Bonded Complexes" [J. Chem. Phys. 119, 12129 (2003)]. *J. Chem. Phys.* **2004**, *121*, 11507. [CrossRef]
93. Jensen, K.P. Bioinorganic Chemistry Modeled with the TPSSh Density Functional. *Inorg. Chem.* **2008**, *47*, 10357–10365. [CrossRef]
94. Roy, L.E.; Hay, P.J.; Martin, R.L. Revised Basis Sets for the LANL Effective Core Potentials. *J. Chem. Theory Comput.* **2008**, *4*, 1029–1031. [CrossRef] [PubMed]
95. Weigend, F.; Ahlrichs, R. Balanced Basis Sets of Split Valence, Triple Zeta Valence and Quadruple Zeta Valence Quality for H to Rn: Design and Assessment of Accuracy. *Phys. Chem. Chem. Phys.* **2005**, *7*, 3297–3305. [CrossRef] [PubMed]
96. Soda, T.; Kitagawa, Y.; Onishi, T.; Takano, Y.; Shigeta, Y.; Nagao, H.; Yoshioka, Y.; Yamaguchi, K. Ab Initio Computations of Effective Exchange Integrals for H–H, H–He–H and Mn_2O_2 Complex: Comparison of Broken-Symmetry Approaches. *Chem. Phys. Lett.* **2000**, *319*, 223–230. [CrossRef]